A&A 390, 533–553 (2002)
DOI: 10.1051/0004-6361:20020603

Astronomy & Astrophysics

The carrier of the "30" μm emission feature in evolved stars⋆,⋆⋆

A simple model using magnesium sulfide

S. Hony[1], L. B. F. M. Waters[1,2], and A. G. G. M. Tielens[3,4]

[1] Astronomical Institute "Anton Pannekoek", Kruislaan 403, 1098 SJ Amsterdam, The Netherlands
[2] Instituut voor Sterrenkunde, K.U. Leuven, Celestijnenlaan 200B, 3001 Heverlee, Belgium
[3] SRON Laboratory for Space Research Groningen, PO Box 800, 9700 AV Groningen, The Netherlands
[4] Kapteyn Astronomical Institute PO Box 800, 9700 AV Groningen, The Netherlands

Received 4 March 2002 / Accepted 16 April 2002

Abstract. We present 2−45 μm spectra of a large sample of carbon-rich evolved stars in order to study the "30" μm feature. We find the "30" μm feature in a wide range of sources: low mass loss carbon stars, extreme carbon-stars, post-AGB objects and planetary nebulae. We extract the profiles from the sources by using a simple systematic approach to model the continuum. We find large variations in the wavelength and width of the extracted profiles of the "30" μm feature. We modelled the whole range of profiles in a simple way by using magnesium sulfide (MgS) dust grains with a MgS grain temperature different from the continuum temperature. The systematic change in peak positions can be explained by cooling of MgS grains as the star evolves off the AGB. In several sources we find that a residual emission excess at ∼26 μm can also be fitted using MgS grains but with a different grains shape distribution. The profiles of the "30" μm feature in planetary nebulae are narrower than our simple MgS model predicts. We discuss the possible reasons for this difference. We find a sample of warm carbon-stars with very cold MgS grains. We discuss possible causes for this phenomenon. We find no evidence for rapid destruction of MgS during the planetary nebula phase and conclude that the MgS may survive to be incorporated in the ISM.

Key words. stars: AGB and post-AGB – stars: carbon – circumstellar matter – stars: mass-loss – planetary nebulae: general – infrared: stars

1. Introduction

The far infrared (IR) spectra of carbon-rich evolved objects; i.e., carbon-rich AGB stars (C-stars), post asymptotic giant branch objects (post-AGBs) and planetary nebulae (PNe) are typified by a broad emission feature around 30 μm. This "30" μm feature was first discovered in the far-IR spectra of CW Leo, IC 418 and NGC 6572 by Forrest et al. (1981). Since then this feature has been detected in a wide range of carbon-rich evolved objects from intermediate mass loss C-stars (Yamamura et al. 1998) to post-AGBs and PNe (Omont 1993; Cox 1993; Omont et al. 1995; Jiang et al. 1999; Szczerba et al. 1999; Hony et al. 2001). The feature is commonly found in C-rich post-AGBs and PNe however with varying band shapes and varying feature to continuum ratios (Goebel & Moseley 1985; Waters et al. 2000; Hrivnak et al. 2000; Volk et al. 2002)

Goebel & Moseley (1985) proposed solid magnesium sulfide (MgS) as the possible carrier of the "30" μm feature. Their suggestion is based on the coincidence of the emission feature with the sole IR-resonance of MgS (Nuth et al. 1985; Begemann et al. 1994) and the fact that MgS is one of the expected condensates around these objects (Lattimer et al. 1978; Lodders & Fegley 1999). Several authors have taken up on this suggestion and compared observations with laboratory measurements of MgS. These comparisons were further facilitated by the publication of the optical constants of MgS in the IR range by Begemann et al. (1994). These authors found that the far IR excess of CW Leo can be successfully modelled using MgS grains with a broad shape distribution.

More recently, Jiang et al. (1999) and Szczerba et al. (1999) have modelled the spectra taken with the Short Wavelength Spectrometer (SWS) (de Graauw et al. 1996) onboard the Infrared Space Observatory (ISO) (Kessler et al. 1996) of the C-star IRAS 03313+6058 and the post-AGB object IRAS 04296+3429 respectively. They find that for these sources which show a strong "30" μm feature, the elemental abundances of Mg and S are consistent with MgS as the carrier of the feature.

Hrivnak et al. (2000) and Volk et al. (2002) have analysed ISO spectra of a sample of post-AGBs. They find that the profile of the "30" μm feature varies between sources. Although

Send offprint requests to: S. Hony, e-mail: hony@astro.uva.nl

⋆ Based on observations obtained with ISO, an ESA project with instruments funded by ESA Member states (especially the PI countries: France, Germany, The Netherlands and the United Kingdom) with the participation of ISAS and NASA.

⋆⋆ Appendix A (Figs. A.1 and A.2) is only available in electronic form at http://www.edpsciences.org

these authors state that this decomposition is not unique, they find that their "30" μm feature is composed of two sub features: one feature peaking near 26 μm and an other near 30 μm. Using these two components in varying relative amounts they are able to explain the range of features found in their sample. Based on the discovery of these sub features they consider the carrier(s) of the "30" μm feature to be unidentified.

Other materials have also been proposed as carriers of the "30" μm feature. Duley (2000) suggests that the "30" μm feature may be indicative of carbon-based linear molecules with specific side groups. Such molecules have strong absorption bands throughout the 15−30 μm range. Papoular (2000) discusses the possible contribution of carbonaceous dust grains with oxygen in the structure. Some of these materials may show IR emission in the 20−30 μm range. Since the optical properties of such grains are sensitive to the exact composition they might be able to explain the range of features found in the C-rich evolved stars. Recently, Grishko et al. (2001) have proposed hydrogenated amorphous carbon (HAC) as a possible carrier of the "30" μm feature.

The ISO mission has provided an excellent database of observations to study the properties of the "30" μm feature in detail and test the suggested identifications *systematically*. The wavelength coverage of the SWS instrument (2–45 μm) is sufficient to determine a reliable continuum. The sensitivity of the ISO spectrograph allows detection of relatively weak features. The resolving power of the instrument ($\lambda/\Delta\lambda$ = 500–1500) makes it feasible to study possible substructure in the "30" μm feature. Thus these observations allow a study of the "30" μm feature in unprecedented detail in a large sample of sources.

In this paper, we investigate the shape and strength of the "30 μm" in a wide range of objects from visual visible C-stars, extreme C-stars, post-AGBs to PNe in order to further test the MgS or other identifications and map systematic differences between the feature in different classes of sources.

Our paper is organised as follows. In Sect. 2, we describe the sample and the data reduction. In Sect. 3, we present the way in which we modelled the continuum in order to extract the feature properties. In Sect. 4, we present the full range of extracted profile shapes and peak positions of the "30" μm feature and we discuss the possible ways of interpreting the observed profiles. In Sect. 5, we develop a simple model using MgS for the "30" μm feature. In Sect. 6, we present the model results and compare them to the astronomical spectra. In Sect. 7, we present a correlation study between several feature properties and stellar parameters. Finally, in Sect. 8, we discuss the implications of our model results and the consequences for the MgS identification. In particular, we discuss possible causes for the deviating profiles and the possibility that MgS produced in carbon-rich evolved stars will be incorporated in the interstellar medium (ISM).

2. Observations

We present observations obtained with ISO of a sample of bright IR sources at different stages along the evolutionary track from C-star via post-AGB object to PN. The observations presented here consist of data obtained with the ISO/SWS

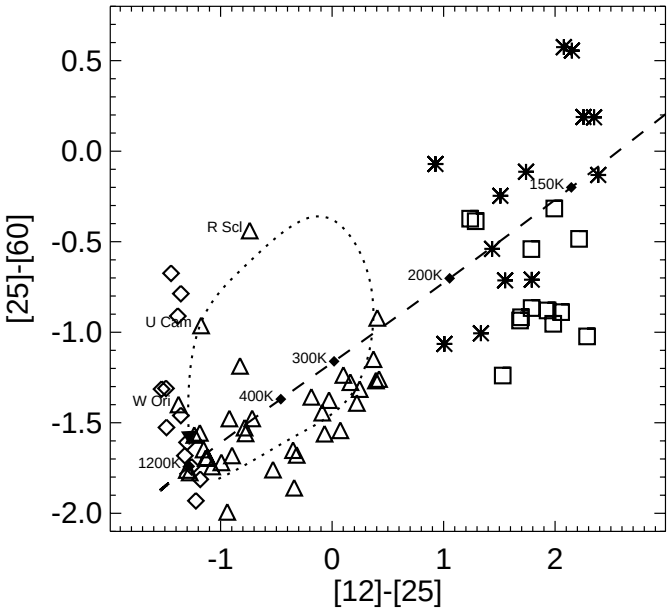

Fig. 1. The IRAS two-colour diagram for the sources studied in this sample. The triangles represent the C-stars, the squares are the post-AGB objects, the stars are the PNe and the diamonds are the C-stars without a "30" μm feature detected. The dashed line represents the position of blackbodies of different temperatures. The dotted line sketches the evolution of a C-star with a detached, expanding and cooling circumstellar shell.

using astronomical observing template 06 and 01 at various speeds. These observing modes produces observations from 2.3 to 45 μm with a resolving power ($\lambda/\Delta\lambda$) ranging from 500 to 1500. The sample consists of all carbon-rich evolved objects in the ISO archive which exhibit a "30" μm feature stronger than 8 Jy peak intensity and have been observed over the full 2.3−45.2 μm wavelength range of the ISO/SWS. This peak intensity and the typical noise level of SWS band 4 (29−45.2 μm) allows to extract a reasonably reliable feature strength and profile. The complete wavelength coverage is needed in order to provide a sufficient baseline to estimate the continuum. We have further completed the sample with all observed C-stars with an IRAS 25 μm flux over 13 Jy. These sources serve as a control group since we would expect to detect the "30" μm feature based on this brightness, the typical noise levels and the typical feature over continuum level. These sources without the "30" μm feature detected are listed separately in Table 1. It should be emphasised that the ISO archive does not contain a statistically representative sample of objects. The database of observations for the carbon stars provides a reasonable sampling over stellar properties (e.g. mass-loss rates or colour temperatures). However the post-AGB sample is heavily biased towards the "21" μm objects; a peculiar type of C-rich post-AGB object. The sample of PNe contains a collection of either bright, well-known or well-studied objects without a proper statistical selection. It also contains a relatively large proportion of PNe with hydrogen-poor central stars. The total sample of 75 sources contains 48 C-stars, 14 post-AGB objects and 13 PNe. We have detected the "30" μm feature in 36 out of 48 C-stars.

Table 1. Source list. Observational details of the sources in this study.

Object	IRAS name	Obs.[a] Mode	α (J2000)	δ (J2000)	TDT[b]	Sp./T kK	Obj. Type
NGC 40	00102+7214	01(3)	00 13 01.10	+72 31 19.09	30003803	WC	PN
IRAS 00210+6221	00210+6213	01(1)	00 23 51.20	+62 38 07.01	40401901		C-star
IRAS 01005+7910	01005+7910	01(2)	01 04 45.70	+79 26 47.00	68600302	OBe	post-AGB
HV Cas	01080+5327	01(1)	01 11 03.50	+53 43 40.30	62902503		C-star
RAFGL 190	01144+6658	01(2)	01 17 51.60	+67 13 53.90	68800128		C-star
R Scl[†]	01246−3248						C-star
–		01(2)	01 26 58.10	−32 32 34.91	37801213		
–		01(2)	01 26 58.05	−32 32 34.19	37801443		
IRAS Z02229+6208	Z02229+6208	01(1)	02 26 41.80	+62 21 22.00	44804704	G0	post-AGB
RAFGL 341	02293+5748	01(1)	02 33 00.16	+58 02 04.99	80002450		C-star
IRC+50 096	03229+4721	01(2)	03 26 29.80	+47 31 47.10	81002351		C-star
IRAS 03313+6058	03313+6058	01(1)	03 35 31.50	+61 08 51.00	62301907		C-star
U Cam	03374+6229	01(2)	03 41 48.16	+62 38 55.21	64001445		C-star
RAFGL 618	04395+3601	01(3)	04 42 53.30	+36 06 52.99	68800561	B0	PN
W Ori	05028+0106	01(3)	05 05 23.70	+01 10 39.22	85801604		C-star
IC 418	05251−1244	01(2)	05 27 28.31	−12 41 48.19	82901301	36[1]	PN
V636 Mon	06226−0905	01(1)	06 25 01.60	−09 07 16.00	86706617		C-star
RAFGL 940	06238+0904	01(2)	06 26 37.30	+09 02 16.01	87102602		C-star
IRAS 06582+1507	06582+1507	01(2)	07 01 08.40	+15 03 40.00	71002102		C-star
HD 56126[†]	07134+1005					F5	post-AGB
–		06	07 16 10.20	+09 59 48.01	71802201		
–		06	07 16 10.30	+09 59 48.01	72201702		
–		01(3)	07 16 10.20	+09 59 48.01	72201901		
CW Leo	09451+1330	06	09 47 57.27	+13 16 42.82	19900101		C-star
NGC 3918	11478−5654	01(1)	11 50 18.91	−57 10 51.10	29900201		PN
RU Vir	12447+0425	01(2)	12 47 18.43	+04 08 41.89	24601053		C-star
IRAS 13416-6243	13416−6243	01(3)	13 45 07.61	−62 58 18.98	62803904		post-AGB
II Lup	15194−5115	06	15 23 04.91	−51 25 59.02	29700401		C-star
V Crb	15477+3943	06	15 49 31.21	+39 34 17.80	25502252		C-star
PN K 2-16[†]	16416−2758					WC	PN
–		01(1)	16 44 49.10	−28 04 05.02	29302010		
–		01(2)	16 44 49.10	−28 04 05.02	67501241		
IRAS 16594-4656	16594−4656	01(1)	17 03 09.67	−47 00 27.90	45800441		post-AGB
NGC 6369	17262−2343	01(1)	17 29 20.80	−23 45 32.00	45601901	WC8[2]	PN
IRC+20 326	17297+1747	01(1)	17 31 54.90	+17 45 20.02	81601210		C-star
CD-49 11554	17311−4924	01(2)	17 35 02.41	−49 26 22.31	10300636	BIIIe	post-AGB
PN HB 5	17447−2958	01(3)	17 47 56.11	−29 59 39.70	49400104		PN
RAFGL 5416	17534−3030	01(1)	17 56 36.90	−30 30 47.02	12102004		C-star
T Dra	17556+5813	01(2)	17 56 23.30	+58 13 06.38	34601702		C-star
RAFGL 2155	18240+2326	01(1)	18 26 05.69	+23 28 46.31	47100261		C-star
IRAS 18240-0244	18240−0244	01(1)	18 26 40.00	−02 42 56.99	14900804	WC	PN
IRC+00 365	18398−0220	01(2)	18 42 24.68	−02 17 25.19	49901342		C-star
RAFGL 2256	18464−0656	01(1)	18 49 10.35	−06 53 03.41	48300563		C-star
PN K 3-17	18538+0703	01(2)	18 56 18.05	+07 07 25.61	49900640		PN
IRC+10 401	19008+0726	01(1)	19 03 18.10	+07 30 43.99	87201221		C-star
IRAS 19068+0544	19068+0544	01(1)	19 09 15.40	+05 49 05.99	47901374		C-star
NGC 6790	19204+0124	01(1)	19 22 57.00	+01 30 46.51	13401107	70[3]	PN
RAFGL 2392	19248+0658	01(1)	19 27 14.40	+07 04 09.98	85800120		C-star
NGC 6826	19434+5024	01(4)	19 44 48.20	+50 31 30.00	27200786	50[4]	PN
IRAS 19454+2920	19454+2920	01(1)	19 47 24.25	+29 28 11.78	52601347		post-AGB
HD 187885	19500−1709	01(2)	19 52 52.59	−17 01 49.58	14400346	F2	post-AGB
RAFGL 2477	19548+3035	01(1)	19 56 48.26	+30 43 59.20	56100849		C-star
IRAS 19584+2652	19584+2652	01(1)	20 00 31.00	+27 00 37.01	52600868		C-star
IRAS 20000+3239	20000+3239	01(1)	20 01 59.50	+32 47 33.00	18500531	G8	post-AGB
V Cyg[†]	20396+4757						C-star
–		01(2)	20 41 18.20	+48 08 29.00	42100111		
–		01(2)	20 41 18.20	+48 08 29.00	42300307		

Table 1. continued.

Object	IRAS name	Obs.[a] Mode	α (J2000)	δ (J2000)	TDT[b]	Sp./T kK	Obj. Type
NGC 7027[†]						200[5]	PN
–		01(4)	21 07 01.71	+42 14 09.10	02401183		
–		01(1)	21 07 01.70	+42 14 09.10	23001356		
–		01(2)	21 07 01.70	+42 14 09.10	23001357		
–		01(3)	21 07 01.70	+42 14 09.10	23001358		
–		01(4)	21 07 01.63	+42 14 10.28	55800537		
S Cep	21358+7823	01(1)	21 35 12.80	+78 37 28.20	56200926		C-star
RAFGL 2688		01(3)	21 02 18.80	+36 41 37.79	35102563	F5	post-AGB
RAFGL 2699	21027+5309	01(1)	21 04 14.70	+53 21 02.99	77800722		C-star
IC 5117	21306+4422	01(1)	21 32 30.83	+44 35 47.29	36701824	77[3]	PN
RAFGL 5625	21318+5631	01(1)	21 33 22.30	+56 44 39.80	11101103		C-star
IRAS 21489+5301	21489+5301	01(1)	21 50 45.00	+53 15 28.01	15901205		C-star
SAO 34504	22272+5435	01(2)	22 29 10.31	+54 51 07.20	26302115	G5	post-AGB
IRAS 22303+5950	22303+5950	01(1)	22 32 12.80	+60 06 04.00	77900836		C-star
IRAS 22574+6609	22574+6609	01(2)	22 59 18.30	+66 25 49.01	39601910		post-AGB
RAFGL 3068	23166+1655	01(2)	23 19 12.48	+17 11 33.40	37900867		C-star
RAFGL 3099	23257+1038	01(1)	23 28 16.90	+10 54 40.00	78200523		C-star
IRAS 23304+6147	23304+6147	01(3)	23 32 44.94	+62 03 49.61	39601867	G2	post-AGB
IRAS 23321+6545	23321+6545	01(1)	23 34 22.53	+66 01 50.41	25500248		post-AGB
IRC+40 540	23320+4316	01(2)	23 34 27.86	+43 33 00.40	38201557		C-star
non detections							
R For	02270−2619	01(1)	02 29 15.30	−26 05 56.18	82001817		C-star
SS Vir	12226+0102	01(1)	12 25 14.40	+00 46 10.20	21100138		C-star
Y CVn	12427+4542	01(2)	12 45 07.80	+45 26 24.90	16000926		C-star
RY Dra	12544+6615	01(3)	12 56 25.70	+65 59 39.01	54300203		C-star
C* 2178	14371−6233	01(1)	14 41 02.50	−62 45 54.00	43600471		C-star
V1079 Sco	17172−4020	01(1)	17 20 46.20	−40 23 18.10	46200776		C-star
T Lyr	18306+3657	06	18 32 19.99	+36 59 55.50	36100832		C-star
S Sct	18476−0758	01(2)	18 50 19.93	−07 54 26.39	16401849		C-star
V Aql	19017−0545	01(2)	19 04 24.07	−05 41 05.71	16402151		C-star
V460 Cyg	21399+3516	01(1)	21 42 01.10	+35 30 36.00	74500512		C-star
PQ Cep	21440+7324	01(1)	21 44 28.80	+73 38 03.01	42602373		C-star
TX Psc	23438+0312	06	23 46 23.57	+03 29 13.70	37501937		C-star

[a] SWS observing mode used (see de Graauw et al. 1996). Numbers in brackets correspond to the scanning speed.
[b] TDT number which uniquely identifies each ISO observation.
[†] These spectra have been obtained by co-adding the separate SWS spectra also listed in the table, see text.
Effective temperatures from [1]Mendez et al. (1992), [2]Perinotto (1991), [3]Kaler & Jacoby (1991), [4]Quigley & Bruhweiler (1995) and [5]Latter et al. (2000).

We present in Fig. 1 the IRAS two-colour diagram for the sources in our sample following van der Veen & Habing (1988). There are four sources in our sample without an entry in the IRAS point source catalogue. For these sources we have used ISO/SWS and LWS observations at 12, 25, 60 and 100 μm to calculate the IRAS colours. For IRAS Z02229, no measurements at 60 and 100 μm are available. In Fig. 1, the warmest sources are located in the lower left corner. These are the optically visible carbon stars with a low present-day mass-loss rate ($\dot{M} \simeq 10^{-8}$–$10^{-7}\,M_{\odot}$). With increasing mass loss the stars become redder and move up and to the right. After the AGB, when the mass loss has terminated, the dust moves away from the star and cools; i.e., these sources move further to the top-right corner of the diagram. The C-stars located above the main group of C-stars have a clear 60 μm excess. This is evidence for an additional cool dust component. Some of these sources are known to have an extended or detached dust shell around them (Young et al. 1993). The empty region between the C-stars and the post-AGBs is physical. When the mass loss stops the star quickly loses its warmest dust and within a short time span (<1000 yr) the star moves to the right in the two-colour diagram. Notice how the sources without a detected "30" μm feature cluster on the left of the diagram, i.e., among the warmest C-stars.

2.1. Data reduction

The SWS data were processed using SWS interactive analysis product; IA[3] (see de Graauw et al. 1996) using calibration files and procedures equivalent with pipeline version 10.1. Further data processing consisted of extensive bad data removal primarily to remove the effects of cosmic ray hits and rebinning on a fixed resolution wavelength grid. If a source has been observed multiple times and these observations are of similar

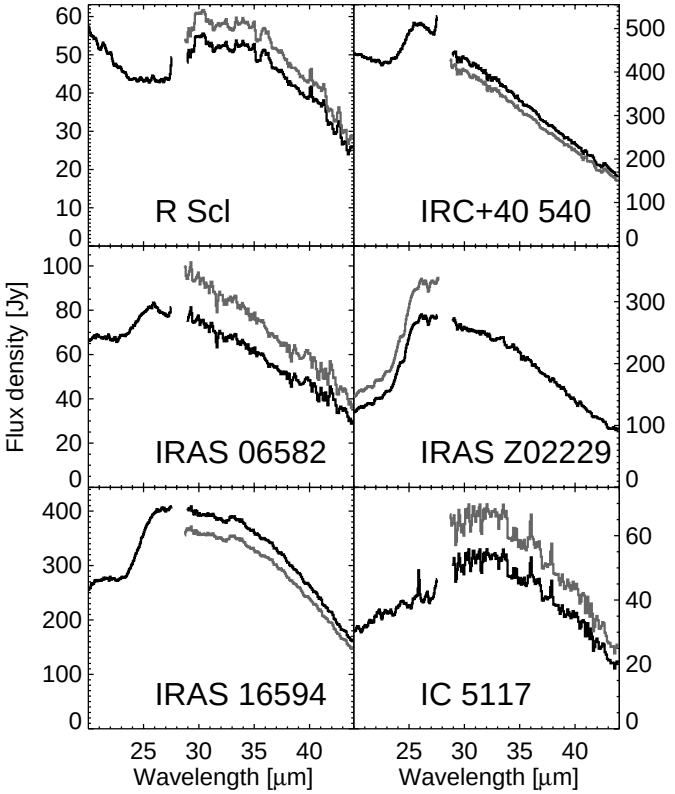

Fig. 2. Examples of the splicing of the SWS band 3D (19.5−27.5 μm) and 4 (28.9−45.2 μm) data. We show the data before (grey line) and after splicing (black line). All data have been scaled to form a continuous spectrum. As can be seen; after splicing, the slope of band 3D and band 4 match. We do not show the band 3E data. The sharp rise at 27 μm in R Scl and IRC+40 450 is an instrumental artifact (see text for details).

quality and of comparable flux-level these data are co-added after the pipeline reduction. These sources are indicated in Table 1 with a dagger (†). Since the features we discuss here are fully resolved in all observing modes, we combine the data obtained in all different modes to maximise the S/N. Although the wavelength coverage of the SWS instrument is well suited to study the profile of the "30" μm feature, there are some important instrumental effects which hamper the unbiased extraction of the emission profiles. We discuss these below.

2.1.1. Splicing

One complete SWS AOT01 spectrum is obtained in 12 different subbands. These subbands are observed through 3 different rectangular apertures which range in size from $14'' \times 20''$ at the shortest wavelengths to $20'' \times 33''$ at the longest wavelengths. All these data are independently flux calibrated and need to be combined to form one continuous spectrum for one source. We apply scaling factors to combine the different subbands to obtain the continuous spectra. The C-stars and post-AGB objects we present in this study all have a small angular extent even compared to the smallest aperture used. Therefore we don't expect large jumps to be present due to the differences between the apertures used. The angular extent of some PNe can be large compared to the sizes of the apertures. If there is a clear indication of flux jumps due to aperture changes we have not included the source in our sample.

2.1.2. Leakage

At wavelengths longer than between 26 and 27.5 μm the data of SWS subband 3D are affected by leakage adding flux from the 13 μm region. The sources used to derive the instrumental response function are all stellar sources without circumstellar material. These calibration sources are all very blue and emit much more flux at 13 μm relative to 26 μm than the cool, red sources we present in this study. Therefore these calibrators are more affected by the leakage than our sources. The instrumental response function derived in this way has been implicitly corrected for leakage for the blue sources. This resulted in fluxes in red sources to be systematically underestimated. More recent calibrations (≥OLP 10.0), have been corrected for this effect. With the improved calibrations, the resulting slopes of the spectra beyond 26 μm have been checked and are in general agreement with the slope of subband 4.

2.1.3. The 27.0–27.5 and 27.5–29.0 μm region

At wavelengths longer than 27.0 μm the data of subband 3D show a sharp increase which is found throughout the complete database of ISO/SWS observations independent of source type. The data of subband 3E (27.5–29.0 μm) are generally unreliable both in shape and absolute flux level. These combined instrumental effects make it inherently difficult to interpret the 27–29 μm spectra. Any substructure detected solely in this region alone should be distrusted.

The instrumental effects between 27 and 29 μm and the fact that each of the subbands is independently flux calibrated make it necessary to devise a strategy for splicing the band 3D, 3E and 4 data. There is unfortunately no objective way to choose this strategy. We choose to assume minimal spectral structure between the end of subband 3D and the beginning of band 4, i.e. to splice the subband 3D−4 data in such a way that the matching slopes of 3D and 4 also match in flux level. Some examples are shown in Fig. 2. The observed discontinuities between subbands are relatively small (<20 per cent) and can be understood as the result of absolute flux calibration uncertainties alone.

2.2. Full spectra

The resultant spectra for the sources that exhibit a "30" μm feature are shown in Figs. 3, 4. The SWS spectra of this large group of objects show a spectacular range in colour temperature, molecular absorption bands and solid state features. The C-stars have molecular absorption bands of C_2H_2 at 3.05, 7−8 and 14 μm, of HCN at 7 and 14 μm, CO at 4.7 μm and C_3 at 4.8−6 μm. The sharp absorption band at 14 μm is due to C_2H_2 and HCN. There is an emission feature due to solid SiC at 11.4 μm. In the reddest C-stars, we find the SiC in absorption. We also find evidence for a weak depression in the 14−22 μm

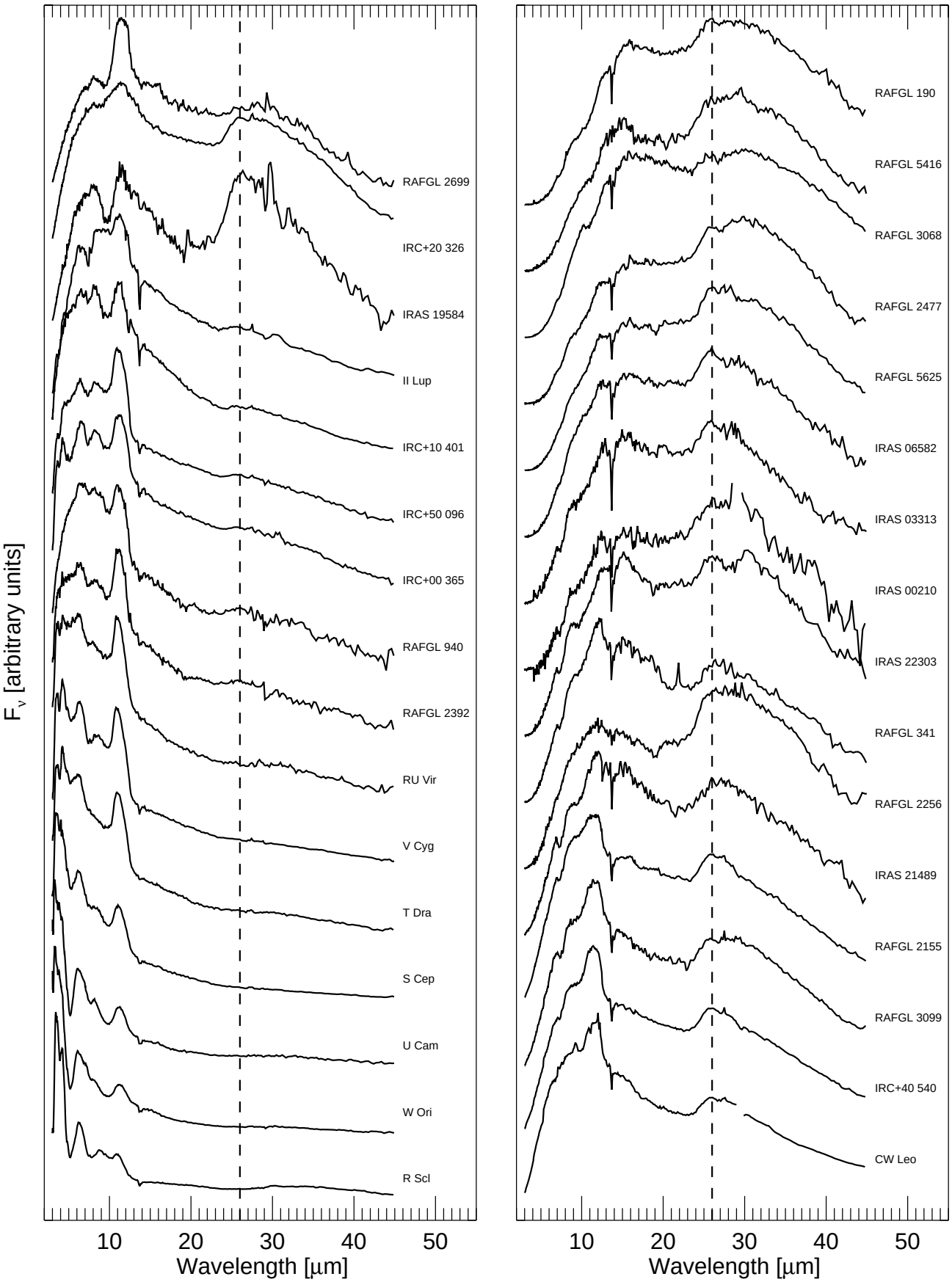

Fig. 3. Overview of the spectra of carbon stars exhibiting the "30" μm feature. The spectra are ordered according to continuum temperature from high to low temperature, bottom to top, left to right. The dashed line marks $\lambda = 26$ μm.

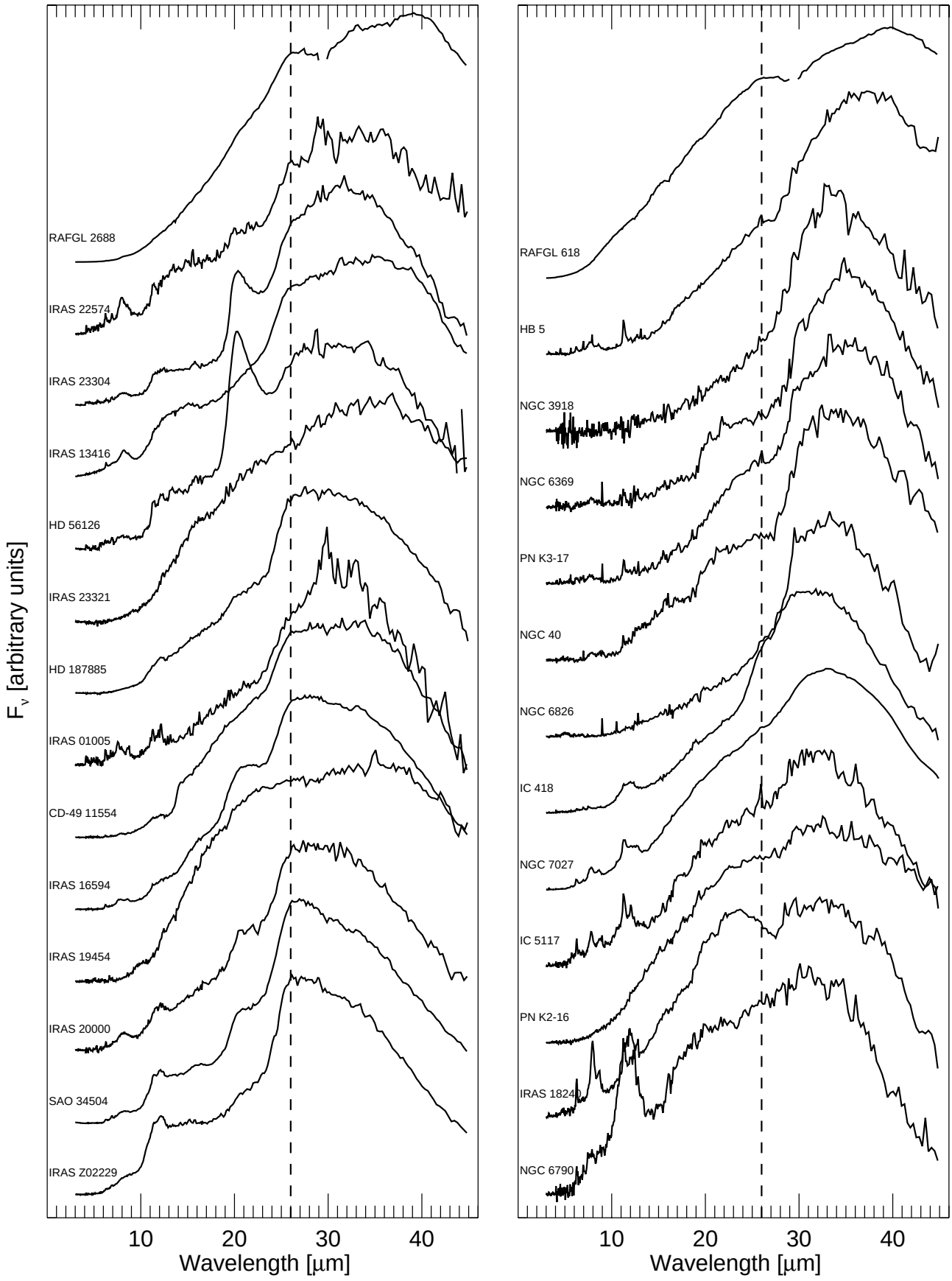

Fig. 4. Overview of the spectra of post-AGB objects (left panel) and PNe (right panel) exhibiting the "30" μm feature. The spectra are ordered according to continuum temperature from high to low temperature, bottom to top. The dashed line marks $\lambda = 26$ μm. The spectrum of RAFGL 618 although warmer than NGC 3918 is shown at the top of the PNe for clarity.

range in the reddest objects. This depression could be due to aliphatic chain molecules like those found in RAFGL 618 (Cernicharo et al. 2001).

The post-AGBs and PNe exhibit many, sometimes broad solid state emission features. In many sources we find emission due to polycyclic aromatic hydrocarbons in the 3–15 μm range. There is a broad plateau feature from 10−15 μm which may be due to hydrogenated amorphous carbon (Guillois et al. 1996; Kwok et al. 2001). Many post-AGBs and two PNe in the sample have a feature peaking at 20.1 μm, called the "21" μm feature in the literature. Recently the carrier of this feature has been identified with TiC (von Helden et al. 2000). The feature at 23 μm found in IRAS 18240 and PN K3-17 is likely due to FeS (Hony et al. 2002). These absorption and emission features have to be taken into account when determining the profile of the "30" μm feature or the shape of the underlying continuum.

Focusing on the "30" μm feature we can see variations in the strength and shape of the band. The most marked difference is however a shift in the peak position going from 26 μm in some of the AGB stars to 38 μm in the PNe. The dashed line in Figs. 3 and 4 indicates $\lambda = 26$ μm. There are systematic changes in the appearance of the "30" μm feature from the C-stars to the PNe. The feature in the C-stars almost exclusively peaks at 26 μm. There are some exceptions like R Scl. In the post-AGB sample, the feature is broader and in some sources the feature peaks long ward of 26 μm. In the PNe sample, there are *no* sources that peak at 26 μm. However, the appearance of a broad feature like the "30" μm feature is sensitive to the shape of the underlying dust continuum, especially since we have a sample with such a wide range of continuum colour temperatures.

3. Continuum

In order to extract the profiles of the "30" μm features and compare them from source to source, we model the underlying continuum due to the emission of other circumstellar (CS) dust components. First, we present the way we construct these continua and in Sect. 4, we discuss the resulting profiles.

To model the underlying continuum we use a simplified approach. We represent the continuum with a single temperature modified blackbody,

$$F(\lambda) = A \times B(\lambda, T) \times \lambda^{-p}, \quad (1)$$

where λ is the wavelength, $F(\lambda)$ is the flux density of the continuum, $B(\lambda, T)$ is the Planck function of temperature T, p is the dust emissivity index and A is a scaling factor.

We have chosen this approach to estimate the continuum over doing a radiative transfer calculation for reasons of simplicity. The bulk of the CS dust around these sources consists of some form of amorphous carbon grains that do not exhibit sharp emission features in the wavelength range of interest. Therefore, a radiative transfer calculation will not yield extra insight into the shape or strength of the continuum while introducing many more modelling parameters. This method has the advantage that we can compare the feature in such a diverse group of sources in a consistent way. Of course Eq. (1) does not directly allow us to incorporate important effects such as optical depth or temperature gradients. However varying the p-parameter can mimic these effects to some extent.

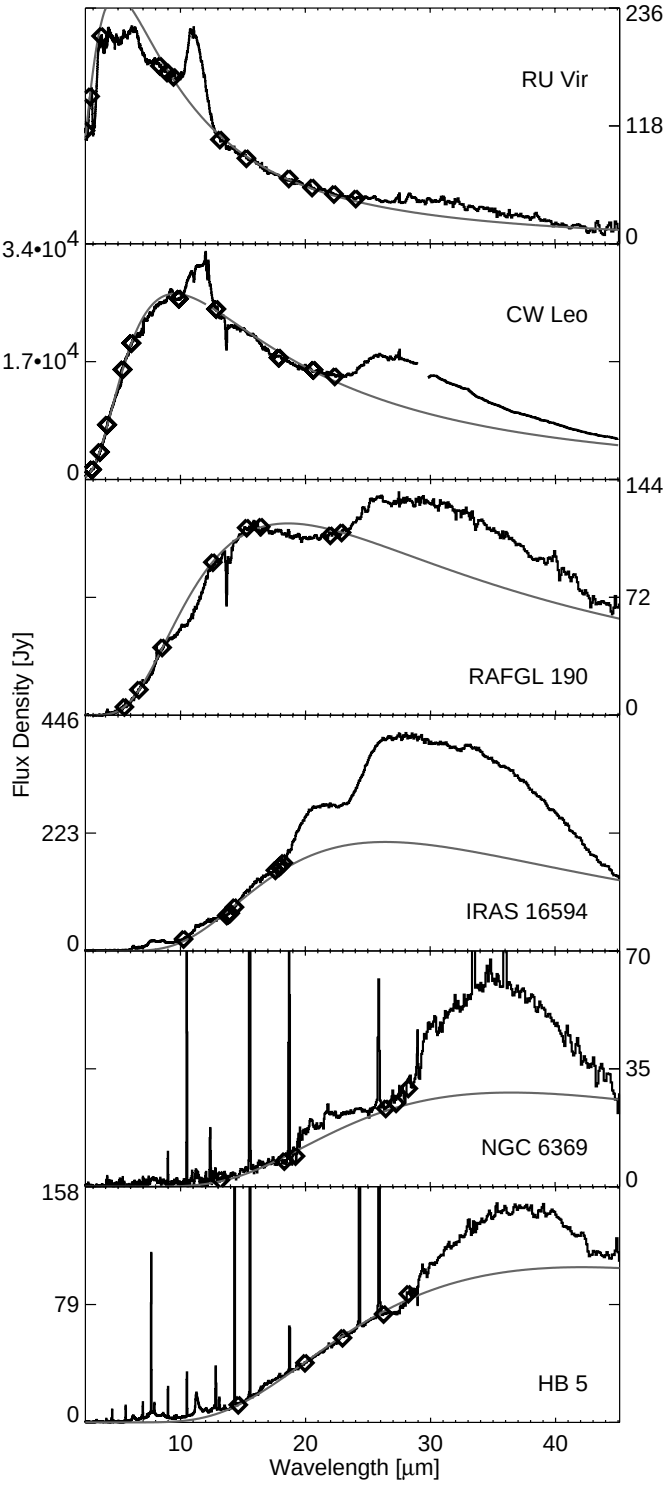

Fig. 5. Examples of the fitted continuum. We show the spectra (black line), the selected continuum points (diamonds) and the fitted modified blackbody (grey line).

The p-parameter reflects the efficiency with which the dust grains can emit at wavelengths larger than the grain size. Reasonable values of p in the region of interest are between 1 and 2. Crystalline materials have this value close to 2 and

Table 2. Measured properties. $T_{\rm cont}$, p are the parameters of the modified blackbody function fitted to the continuum. $\lambda_{\rm c,30}$ and P/C are the feature centroid position and peak over continuum ratio. $T_{\rm MgS}$ is the derived temperature of the MgS grains.

	cont.		"30" μm feature						cont.		"30" μm feature				
Object	$T_{\rm cont}$	p	$\lambda_{\rm c,30}$	*fwhm*	flux	P/C	$T_{\rm MgS}$	Object	$T_{\rm cont}$	p	$\lambda_{\rm c,30}$	*fwhm*	flux	P/C	$T_{\rm MgS}$
	[K]		[μm]	[μm]	[W/m^2]		[K]		[K]		[μm]	[μm]	[W/m^2]		[K]
NGC 40	150	0	33.6	10.1	5.9e-13	0.7	110	T Dra	1210	0	30.2	10.1	4.8e-13	0.4	200
IRAS 00210	285	0.5	28.4	10.7	6.4e-13	0.8	300	RAFGL 2155	460	0	28.8	8.2	5.7e-12	0.6	400
IRAS 01005	130	1	30.0	11.1	6.6e-13	1.5	220	IRAS 18240	160	1	32.8	13.1	1.0e-12	1.0	130
HV Cas	1040	0.2	33.5	10.6	1.5e-13	0.3	100:	IRC+00 365	910	−0.3	28.6	11.7	1.9e-12	0.4	500
RAFGL 190	275	0	30.9	13.0	1.6e-12	0.3	180	RAFGL 2256	390	0	29.5	12.0	1.9e-12	1.0	350
R Scl	2605	−0.2	33.2	13.9	1.1e-12	1.1	90	K3-17	100	1	34.1	11.5	1.0e-12	0.9	90
IRAS Z02229	235	0	29.1	10.1	8.3e-12	1.7	300	IRC+10 401	765	0	30.0	10.0	2.0e-12	0.3	300
RAFGL 341	380	0	29.8	9.4	9.4e-13	0.4	250	IRAS 19068	1165	−0.7	28.5	10.1	2.0e-13	0.4	500:
IRC+50 096	855	−0.2	28.8	9.2	1.9e-12	0.3	500	NGC 6790	290	0	29.8	15.6	9.8e-13	1.4	300
IRAS 03313	325	0	28.6	7.8	5.4e-13	0.4	300	RAFGL 2392	890	0	27.7	8.6	3.4e-13	0.5	500
U Cam	1775	0	31.9	11.8	3.9e-13	0.6	150	NGC 6826	150	0	32.7	10.5	1.1e-12	2.0	120
RAFGL 618	235	−1	38.0	10.9	5.4e-12	0.2	40[a]	IRAS 19454	140	1	36.3	13.1	6.4e-13	0.3	50
W Ori	2450	0	31.3	8.4	3.1e-13	0.4	150	HD 187885	175	0	29.6	10.8	5.2e-12	1.0	200
IC 418	120	1	30.8	11.3	5.5e-12	0.9	180	RAFGL 2477	290	0	30.7	12.5	2.3e-12	0.6	170
V636 Mon	1215	0	29.8	10.1	1.7e-13	0.2	250:	IRAS 19584	580	0	28.1	7.5	8.5e-13	1.5	400
RAFGL 940	810	0	28.2	10.2	3.5e-13	0.5	500	IRAS 20000	210	0	29.4	12.1	2.5e-12	1.5	300
IRAS 06582	315	0	29.5	10.3	1.1e-12	0.4	300	V Cyg	1110	0	30.5	11.5	1.3e-12	0.3	200
HD 56126	170	0	30.0	12.0	2.9e-12	0.8	150	NGC 7027	125	1	32.8	11.0	1.7e-11	0.4	110
CW Leo	535	0	28.6	8.8	2.7e-10	0.6	400	S Cep	1340	0.1	31.2	9.4	4.4e-13	0.2	130
NGC 3918	90	1	33.3	8.5	7.1e-13	1.0	120	RAFGL 2688	200	−1	31.1	10.4	5.9e-11	0.3	70[a]
RU Vir	1045	0	30.4	10.1	5.3e-13	0.6	180	RAFGL 2699	540	0	29.0	11.4	5.9e-13	0.7	300
IRAS 13416	115	1	31.6	15.8	2.8e-12	0.4	200[a]	IC 5117	130	1	31.2	9.7	7.3e-13	0.6	150
II Lup	625	0	29.5	10.1	3.9e-12	0.3	400	RAFGL 5625	300	0	30.3	11.8	4.4e-12	0.4	200
V Crb	1430	0	30.4	10.1	1.8e-13	0.3	150:	IRAS 21489	415	0	29.3	9.7	1.1e-12	0.6	350
K2-16	155	0.5	34.4	12.0	3.4e-13	0.3	80	SAO 34504	210	0	29.1	10.3	1.3e-11	2.0	250
IRAS 16594	140	1	29.8	12.1	9.9e-12	0.9	250	IRAS 22303	345	0	30.3	10.5	1.0e-12	0.7	300
NGC 6369	100	1	34.6	10.1	9.5e-13	1.1	90	IRAS 22574	160	0	31.2	13.6	5.9e-13	0.4	150
IRC+20 326	770	−0.7	29.1	10.2	7.4e-12	0.5	300	RAFGL 3068	290	0	32.4	14.7	8.4e-12	0.4	120
CD-49 11554	140	1	30.2	14.0	4.7e-12	0.7	200[a]	RAFGL 3099	470	0	29.5	10.9	2.6e-12	0.7	400
HB 5	120	0	35.5	11.5	1.0e-12	0.4	70	IRAS 23304	115	1	30.1	13.4	2.3e-12	1.1	250
RAFGL 5416	290	0	30.4	12.5	2.2e-12	0.5	220	IRAS 23321	175	0	34.5	13.3	6.6e-13	0.3	70
IRC+40 540	485	0	28.6	9.1	8.9e-12	0.6	400								
non detections															
R For	1215	0	-	-	<1e-14	<0.1	-	T Lyr	3305	0	-	-	<1e-14	<0.1	-
SS Vir	2040	0	-	-	<1e-14	<0.1	-	S Sct	2105	0	-	-	<4e-14	<0.3	-
Y CVn	2200	0	-	-	<2e-13	<0.2	-	V Aql	3665	−0.3	-	-	<1e-14	<0.1	-
RY Dra	2525	0	-	-	<1e-13	<0.2	-	V460 Cyg	2875	0	-	-	<5e-14	<0.5	-
C* 2178	1110	0	-	-	<1e-13	<0.5	-	PQ Cep	1625	0	-	-	<1e-14	<0.1	-
V1079 Sco	3085	−0.5	-	-	<5e-14	<0.2	-	TX Psc	3105	0	-	-	<3e-14	<0.1	-

[a] Temperature determination uncertain due to optically thick MgS emission.

amorphous materials have a p-value between 1 and 2, while layered materials have an emissivity index close to 1. A temperature gradient in the dust shell will result in a broader spectral energy distribution (SED). This is mimicked by a lower value of p. Likewise an optically thick dust shell will result in a broader SED, which again can be reproduced by reducing the value of p.

We use a χ^2 fitting procedure to determine the values of T and p fitted to selected continuum points in the ranges 2−22 μm. If available we also use the LWS spectra to verify the continuum at the long wavelength end of the "30" μm feature. The 50−100 μm continuum gives an even stronger constraint on the value of p. For most cases the resultant continuum runs through the 45 μm region of the SWS spectrum. A remarkable exception to this is the spectrum of RAFGL 3068. The 2−24 μm spectrum is well fitted with a single 290 K Planck function. However we find a large excess of this continuum at 45 μm and the available LWS spectrum is not well represented in level or slope. Possibly this is due to the optically thick dust shell or a biaxial dust/temperature distribution.

The values for T and p are listed in Table 2. One remarkable fact is that the C-stars are well fitted by a single temperature

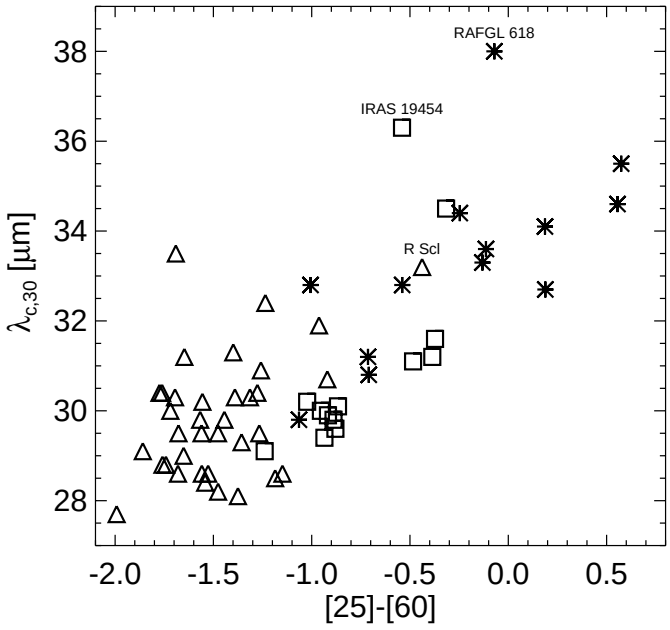

Fig. 6. Centroid of the "30" μm feature with respect to the [25]–[60] colour. The symbols are like in Fig. 1. There is a clear trend for the centroid position of the "30" μm feature to move to longer wavelengths the redder the object is.

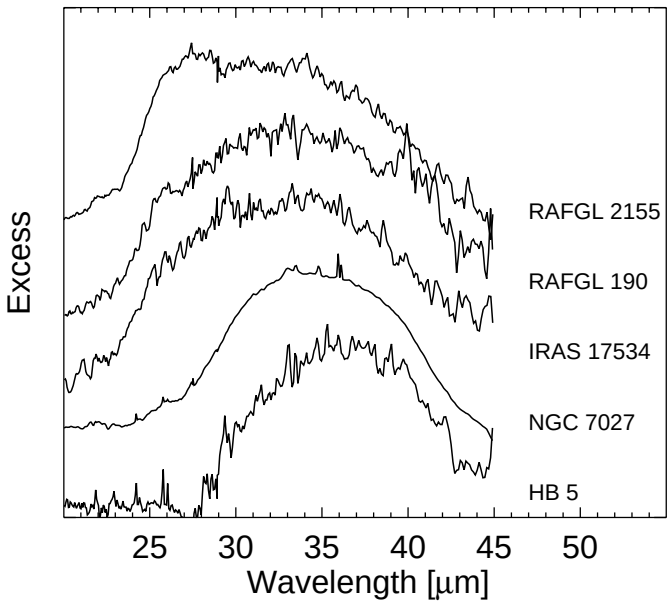

Fig. 7. Emissivities for different sources as deduced from the ISO spectra. There are large differences in the profile of the excess emission. Notice the shift in peak position and change in width of the circumstellar "30" μm feature going from the C-stars to post-AGBs to PNe (top to bottom).

Planck function over the complete wavelength range of SWS. The IR SEDs of the post-AGBs and PNe are in general less broad and many sources are better fitted with a p-value of 1. We stress however that the derived p values cannot be used to constrain the crystal structure or the average size of the dust grains in view of the aforementioned effects of temperature gradients and optical depth.

4. Profiles

Using the continua defined in this way, we measure the following properties of the "30" μm feature: the centroid wavelength ($\lambda_{c,30}$), i.e., the wavelength where the integrated flux in the feature at either side is equal; the full width at half maximum (*fwhm*); the flux in the "30" μm feature and the height of the peak of the "30" μm feature *after* continuum subtraction over the continuum ratio, i.e., the peak to continuum ratio (P/C). The measured values are listed in Table 2. We list upper limits for P/C and the flux for the sources without detection. In Fig. 6, we show the relation between the [25]–[60] colour and $\lambda_{c,30}$. There is a clear reasonably smooth trend for the feature to move to longer wavelengths with redder IRAS colours. This indicates that the temperature of the dust is an important parameter in determining the profile of the "30" μm feature since [25]–[60] is a direct measure of the dust temperature provided that the dust composition in the different sources is similar.

We first try to remove the effect of temperature by dividing by the continuum; a method that is commonly applied. Using the modelled continua as described in Sect. 3, we convert the observed features to relative excess emission by dividing by the continuum and subtracting 1.

If the feature emission is optically thin and the temperature of the carriers of the feature is equal to the continuum temperature the derived excess emissions are proportional to the absorptivity (κ_{abs}) of the carrier and if the carrier is the same in these sources then the derived band shape should be the same for all sources. However, we find large variations in the derived profiles. In Fig. 7, we show some examples of the derived profiles. Most notable are variations in peak position and the appearance around 26 μm. Such changes, albeit within a smaller range of feature peak positions have led other authors (Volk et al. 2000, 2002) to conclude that the "30" μm feature is composed of two features and the observed variations are due to varying relative contributions of these two components. One key question is: "What possible causes could there be for the observed large variations in band shape?". We discuss three possibilities below. First, optical depth effects. Second, temperature effects. Finally, we discuss multiple band carriers.

The optically thin assumption most likely holds because the optical depth in the circumstellar shell strongly decreases towards longer wavelengths. Note, in this respect that the "30" μm feature is never found in absorption (however, see also Sect. 6.2). Hence, optical depth effects are not responsible for the observed profile variations.

Whether the temperature of the amorphous carbon grains (defining the shape of the continuum) and the temperature of the "30" μm carrier are equal is very uncertain. The temperature of a dust grain in a circumstellar envelope is determined by the distance to the star, the absorption properties in the wavelength range where the star or the dust shell emits light and the grain size. In case the temperature of the grains species responsible for the continuum and the "30" μm emission feature are not the same, the resulting excess profiles will also not be the

same from source to source *even if the carrier of the band is the same*. The differences will be very pronounced when the emission feature is broad. In this case systematic difference between sources are bound to occur in league with the strongly changing continuum temperature. Thus, the temperature of the carrier of the "30" μm feature is an important parameter that determines the profile of the emission.

There may be multiple carriers involved as discussed before. In this case the feature near 26 μm dominates in the warmest objects while the cooler objects are more and more dominated by emission towards 35 μm. However, this scenario has its difficulties since it would require changes in the composition of the dust in the relatively dispersed and cold nebular surroundings of a post-AGB object or even during the PN phase. Such chemical changes can only occur extremely slowly, if at all.

Lastly, variations in grain shape or variations in shape distribution can influence the emission profiles. The optical properties of materials with a high value of the refractive index are sensitive to the grain shape. Variations in the shape distribution will lead to variations in the profiles.

In our analysis, we will focus on explaining the profile variations with temperature variations and the effects of variations in the shape distribution of the emitting dust grains.

5. MgS

Since, it has been demonstrated for a few sources that MgS is a viable candidate (Begemann et al. 1994; Jiang et al. 1999; Szczerba et al. 1999), we first test MgS as a possible candidate for the carrier of the feature. With the large sample of good quality spectra in this study we are able to test this possible identification systematically in a large population of evolved objects.

As explained above we cannot derive a priori information on the temperature of the "30" μm carrier from the observations. Our knowledge is further limited by the fact that even for some of the candidate materials like MgS or FeS the optical properties are measured only in a limited wavelength range. We lack measurements in the UV, optical and near-IR range, which may well dominate the dust heating. We have decided to test the MgS identification, leaving the grain temperature as a free parameter. We adopt the method we describe below.

5.1. Material

We use the optical constants as published by Begemann et al. (1994). Of the materials they measured, $Mg_{0.9}Fe_{0.1}S$ is closest to pure MgS. The real and imaginary part of the refractive index (n and k values) are given from 10–500 μm.

5.2. Shapes

From the n and k values we can calculate the absorption cross-sections for various grain shapes and shape distributions in the Rayleigh limit following Bohren & Huffman (1983, Chapters 5, 9 and 12). The absorption cross-section of MgS around 30 μm is very sensitive to the grain shape. In Fig. 8, we show the results of using different grain shapes on the absorption properties of MgS. We use a continuous distribution of ellipsoids (CDE) for the grain shapes. This shape distribution was used by Begemann et al. (1994) and gave a good fit to the "30" μm feature observed in CW Leo. The same shape distribution was further used by Jiang et al. (1999) and Szczerba et al. (1999). They found reasonable fits for the two sources they study. As can be clearly seen in Fig. 8 when comparing the spheres with the CDE calculations, the feature broadens and the peak position shifts to longer wavelengths using the CDE shape distribution. The width of the feature calculated using CDE matches that of the observed "30" μm feature well (e.g. RAFGL 190 in Fig. 8, see also Fig. A.1).

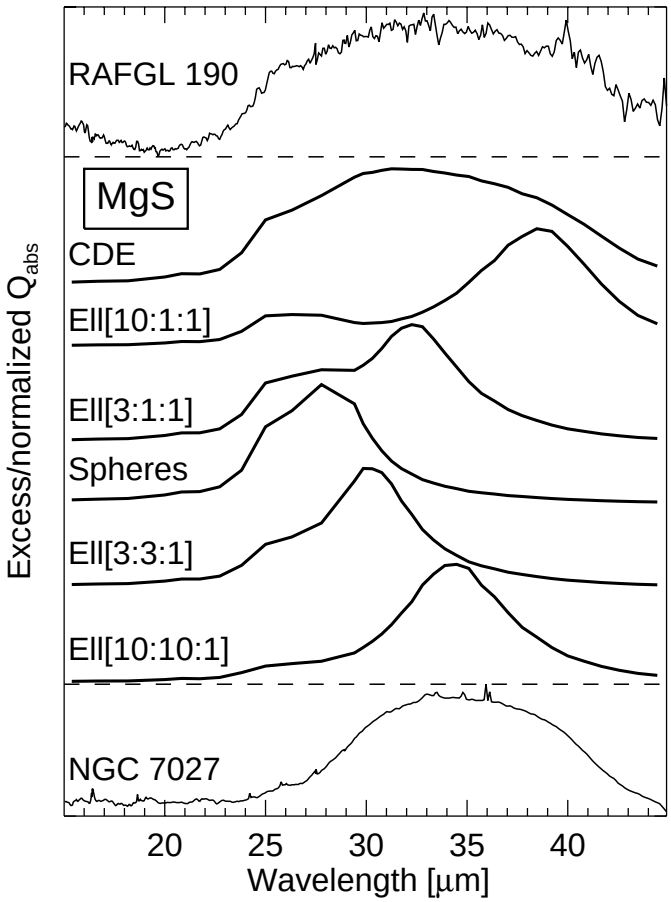

Fig. 8. The effect of grain shape. We show the absorptivity of MgS as a function of grain shape. The numbers between brackets refer to the axis ratios of the elliptical grains. For comparison we show the derived emissivities of RAFGL 190 and NGC 7027.

5.3. Temperature

To estimate the MgS temperature ($T_{\rm MgS}$) we use the continuum *subtracted* spectra with the continuum as derived in Sect. 3. The emission from MgS grains is calculated using the $\kappa_{\rm abs}$ folded with a Planck function with the temperature of the grain. Due to the smooth and broad shape of the resonance the profile of the emission is very sensitive to $T_{\rm MgS}$. In particular the peak position changes strongly with $T_{\rm MgS}$. This allows us to estimate $T_{\rm MgS}$ from the continuum subtracted profiles. This method is

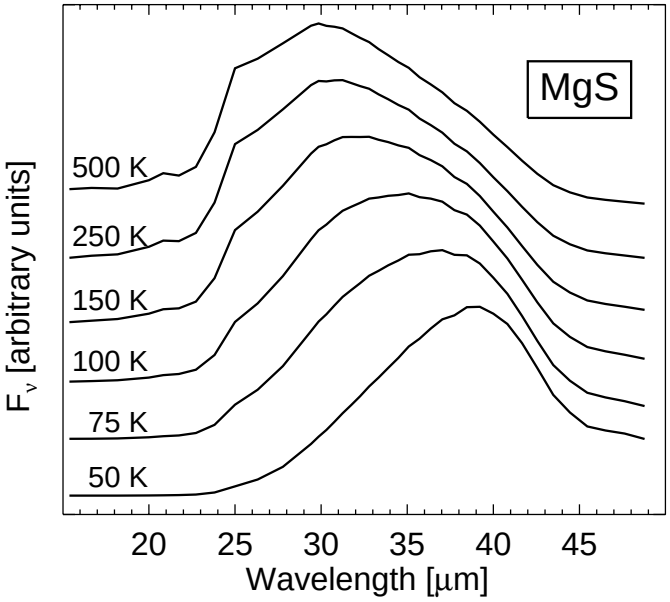

Fig. 9. The effect of grain temperature on the MgS emission feature. We fold the $\kappa_{\rm abs}$ of MgS in a continuous distribution of ellipsoids (CDE) shape distribution with a Planck function of different temperatures. The shape and position of the feature are modified substantially.

most sensitive for $T_{\rm MgS} < 300$ K. Above 300 K, further changes in the profile are more subtle since the major part of the feature falls in the Rayleigh-Jeans domain of the Planck function.

We use this temperature estimate and the observed band strength in the continuum subtracted spectra to synthesise a MgS feature in order to compare with the astronomical spectra. In conclusion, we adopt MgS with a CDE shape distribution and allow both the strength and the temperature of the MgS grains to vary with respect to the underlying continuum.

6. Model results

In Fig. 10 we show a few typical examples of how our model results compare to the observed spectra. In Fig. A.1 we show the observed spectra, the composite of the continuum and the synthetic MgS feature and the residuals after subtracting the MgS feature for the complete sample. The fits are very satisfactory in 50 out of 63 cases. In ~25 sources the synthetic spectra obtained with this very simple model are able to explain the detailed profile of the "30" μm feature very well. The onset and range of the feature and even the slight depression between 26−30 μm are reproduced by the model. We show a zoomed view of the 30 μm region of a few sources that are very well fitted by this simple model in Fig. 11. Notice the different apparent shapes of the feature that the model is able to explain. Volk et al. (2002) discuss the "30" μm feature in IRAS 23304 and find that they need 2 separate unidentified components in order to understand the shape of the feature. Figure 11 illustrates that this is not necessarily required.

Examining the complete sample of observed "30" μm features and the synthetic spectra, we find there are some systematic deviations. In the sample of C-stars and post-AGB objects there are numerous examples where the major part of the "30" μm feature is explained well by our model, but the observed spectra show excess emission in the 26 μm region. The excess is not accounted for using our CDE fits. The most extreme case is IRAS 19584 but several sources exhibit the same behaviour. In Sect. 6.1, we discuss the origin of this discrepancy.

In some cases the synthetic spectra over-predict the flux at the longest wavelengths. This can be due to the very simplistic method we have used to estimate the continuum level. As the dust optical depth decreases with increasing wavelengths, the continuum level estimated from shorter wavelengths might over-predict the true continuum level. Note, however, that the discrepancies between the modelled and the observed spectra in the 26 μm region and the 40 μm region cannot be considered completely independently. If we were to weaken the strength of the MgS feature this would yield a better fit around 45 μm but would increase the discrepancy around 26 μm. We also note that MgS produces a weak continuum contribution at 45 μm (see for example Fig. 9). This continuum contribution is already taken into account when fitting the overall continuum, but it is still present in the calculated MgS contribution. Therefore, our model may slightly over-predict the fluxes near 45 μm.

As a class, the spectra of most PNe show another systematic difference. The peak position of the "30" μm feature lies in general at longer wavelengths than in the post-AGB sources. This is in accordance with the picture of a slowly expanding and cooling dusty envelope. We can simulate the same shift in peak position using MgS grains. However the fits we obtain fail to reproduce the relatively narrow width of the observed profile. We discuss this deviation of the profiles in Sect. 6.3.

There are 4 sources in the sample that have a broader "30" μm feature than can be fit by our simple model. Of these sources, IRAS 13416 and CD-49 11554 show a slightly flattened and broadened feature while in the cases of RAFGL 618 and RAFGL 2688 the feature is very broad with a depression around 30 μm. The latter sources are known to have a very large dust column along the line of sight. Most likely the feature shape is due to optical depth effects. We discuss these sources further in Sect. 6.2.

Despite these systematic deviations it is clear that our simple model is able to explain the profile of the "30" μm feature in good detail in a very wide range of objects. We conclude that the carrier of the "30" μm feature in the C-stars and post-AGB objects is solidly identified with MgS and that *the variations in peak position reflect differences in grain temperature*.

6.1. 26 μm excess

As discussed above we find about 25 sources that are very well fitted by our simple model. Using similar parameters we also find about 25 sources which show an excess near 26 μm. Evidently, there is a contribution from an additional dust component in the latter sources. In considering this additional dust component we find that MgS itself is the best candidate. The wavelength region where this excess occurs (26 μm) is also the wavelength where the generic main resonance of MgS occurs.

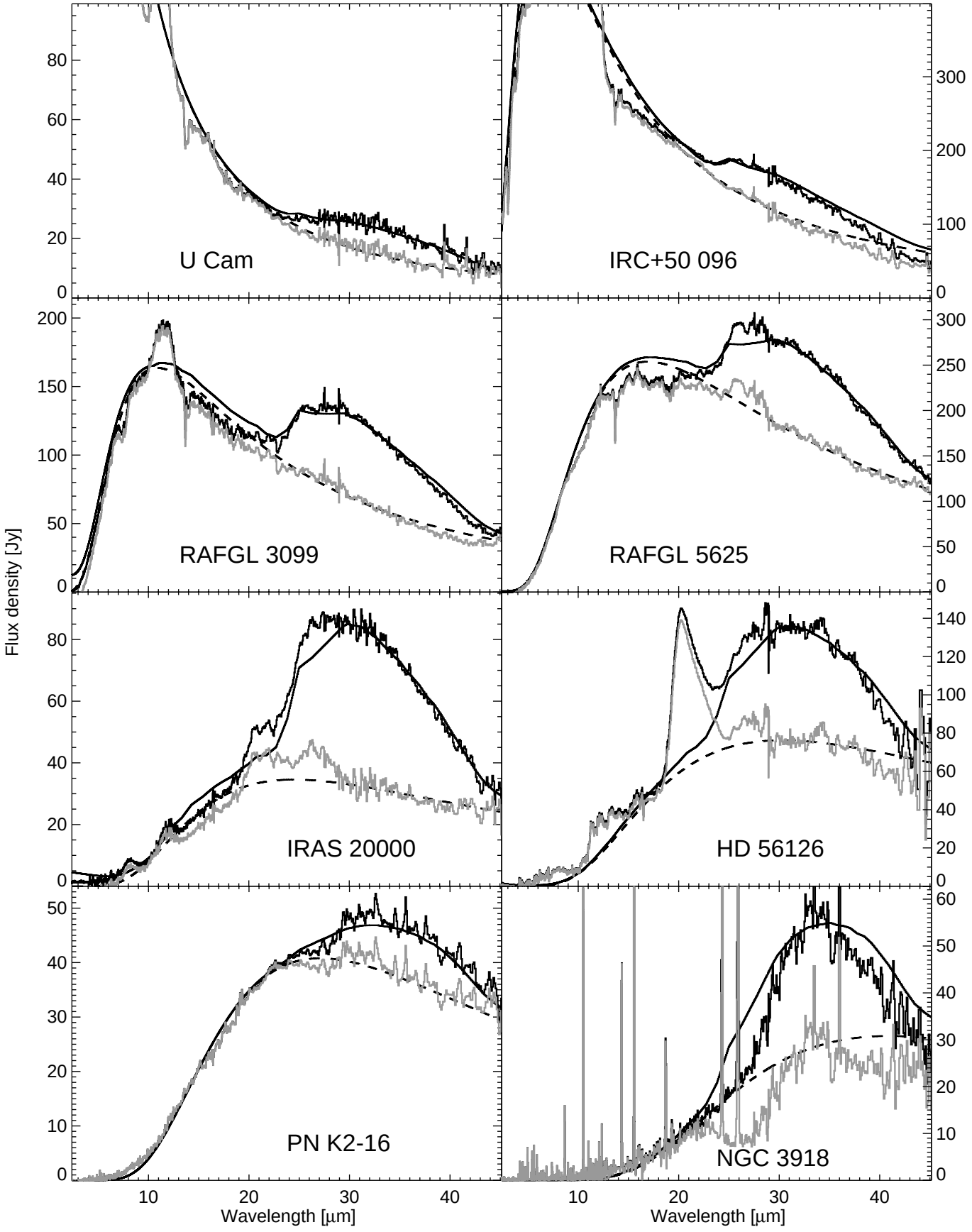

Fig. 10. Examples of the modelling results using measure MgS optical constants in a CDE shape distribution. We show the observed spectra (black), the modelled continua (dashed), the spectra with the MgS contribution subtracted (gray) and the composite of the continuum and the MgS contributions (thin black line).

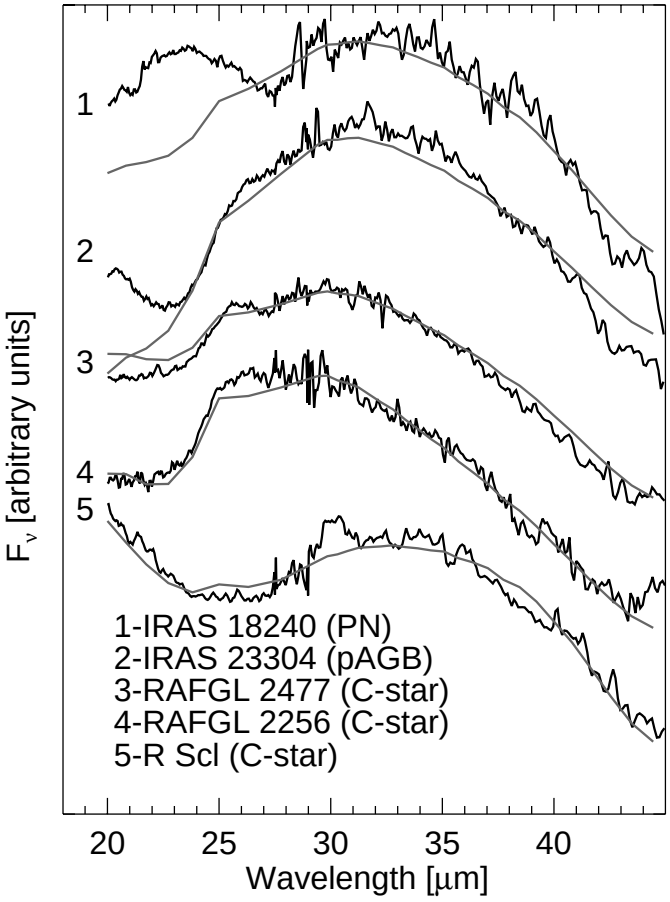

Fig. 11. Examples of spectra that are very well fitted with MgS in a single temperature, CDE shape distribution. The black lines represent the data and the grey line the model. The different sources have been offset for clarity. The excess around 23 μm in IRAS 18240 is due to FeS (Keller et al. 2002; Hony et al. 2002). Notice how the model is able to explain the profile of the "30" μm feature found in the full range of objects in our sample.

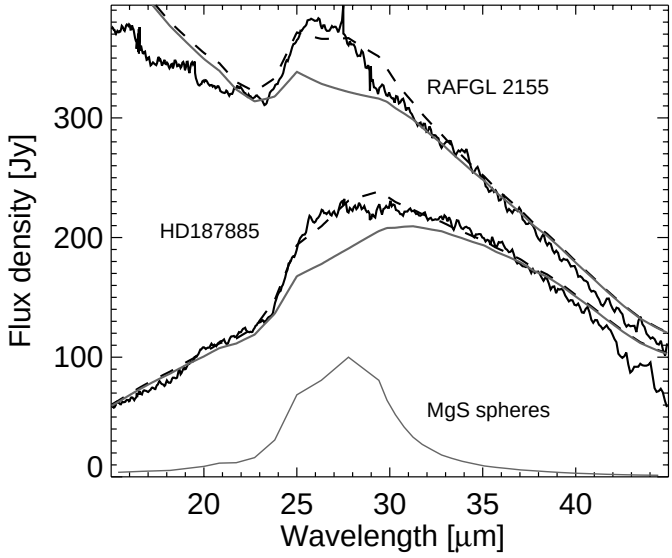

Fig. 12. Some examples of sources with a 26 μm excess compared to the model spectra. We show the data (full black line) the model using the CDE calculation (full grey line) and the composite model using both spherical MgS grains and the CDE calculation (dashed line). We show below the emission of spherical MgS grains at a temperature of 250 K. The continuum in RAFGL 2155 runs above the observed spectrum at the shortest wavelengths, this may be due to molecular absorptions (see Sect. 2.2)

Spherical MgS grains exhibit a resonance at 26 μm. In our model, the MgS profile is broader and peaks at a longer wavelength because we use the calculated absorption cross-sections in a CDE shape distribution. There is no a priori reason why the shape distribution should be close to this distribution. In this respect, it is rather surprising that our simple model works so well for so many sources. We can simulate a different shape distribution by adding the contributions of spherical grains to the CDE profile. This approach is permitted since we assume optically thin emission and thus the contribution of different components add linearly. In Fig. 12, we show the result of such a composite model for one C-star and for one post-AGB object. The relative amounts of spherical grains added to the model is ~35 per cent. We keep the temperature of the spherical and the CDE grains the same as in the initial model. As can be seen the spherical grains contribute at the position where our initial model fails. We conclude that variations in the distribution over grain shapes can explain the variations we observe in the profile of the "30" μm feature.

6.2. Optically thick shells

The feature found in CD-49 11554, IRAS 13416, RAFGL 618 and RAFGL 2688 is different from the others in the sense that it is broader and flatter. This is especially true for RAFGL 618 and RAFGL 2688 where the profile even shows a central depression. We investigate the effect of optical depth on the emission profile. We model the effect of optical depth with two simple limiting cases.

$$I_1(\lambda) = B(\lambda, T_{\rm MgS}) \times (1 - {\rm e}^{-\rho\kappa_\lambda l}) \text{ and} \quad (2)$$

$$I_2(\lambda) = I_0(\lambda, T_{\rm MgS}) \times {\rm e}^{-\rho\kappa_\lambda l}, \quad (3)$$

where $T_{\rm MgS}$ is the temperature of the MgS, $B(\lambda, T)$ is the Planck function of temperature T, ρ is the mass density of MgS, l is the column length and $I_0(\lambda, T)$ is MgS emission of temperature T. $I_1(\lambda)$ is the limiting case of a column of MgS with a single temperature of $T_{\rm MgS}$. $I_2(\lambda)$ represents the case of foreground absorption only; i.e., MgS emission of temperature $T_{\rm MgS}$ obscured by a column of MgS with negligible emission. In both cases the resulting profile will be broader than the optically thin case. For a long column $I_1(\lambda)$ approaches $B(\lambda, T_{\rm MgS})$ while $I_2(\lambda)$ becomes double peaked with a depression where κ_λ peaks. The resulting $I_1(\lambda)$ profile will never show a central depression. We show the effects of incorporating the optical depth in Fig. 13. Indeed, these methods yield a broadened profile closer to what is observed. The second method reproduces the central depression found in RAFGL 2688. It is important to stress that the curves shown in Fig. 13 are not the result of a proper radiative transfer modelling of the CS shell or an attempt to fit the observed spectrum of the source. Nevertheless, they are able to

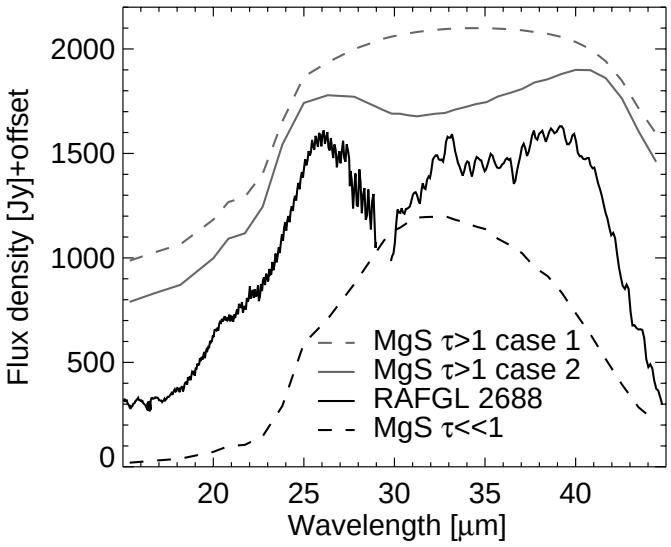

Fig. 13. The effects of optical depth of the profile of the MgS emission. We show the absorbed MgS emission following Eqs. (2) and (3) (grey dashed and solid lines), the profile of the "30" μm feature of RAFGL 2688 (solid black line) and the optically thin MgS emission (dashed black line).

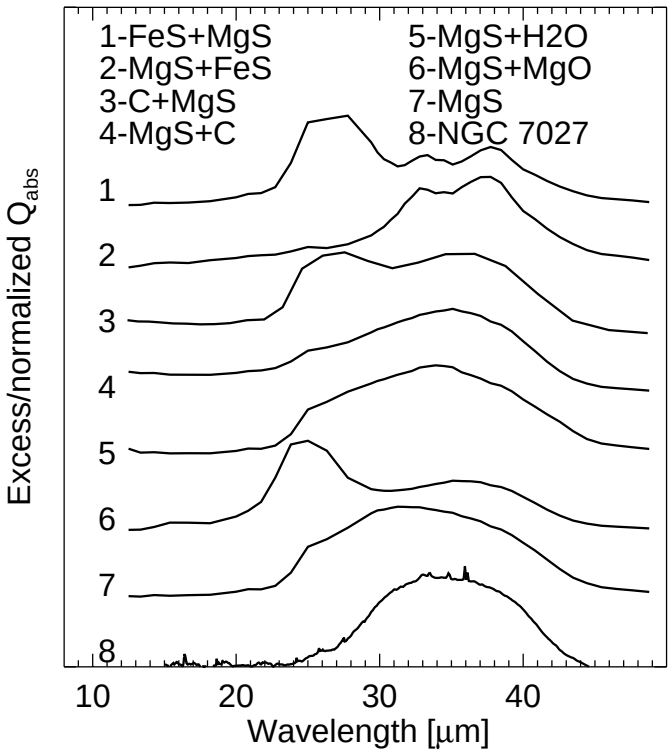

Fig. 14. The absorptivity of MgS grains coated with various types of materials. The modelled grains are composed of 80 per cent MgS and 20 per cent coating by volume. The models have been obtained by adding 5 ellipsoidal core-mantle grain of axes ratios (10:1:1), (3:1:1), (1:1:1), (3:3:1) and (10:10:1) of equal volume. For comparison we show the absorptivity of MgS in a CDE distribution (7) and the excess in NGC 7027 (8). We show the absorptivity of FeS (1) and amorphous carbon (5) grains with a MgS coating, both with core volume of 20 per cent of the grain. None of the modelled composite grains is able to explain the profile of the emission found in many PNe.

explain the general characteristics of the "30" μm profile in the deviant sources well.

6.3. PNe profiles

For 9 out of 13 PNe the observed "30" μm feature is much narrower than in our model. Of the other four cases we discussed the profile of RAFGL 618 in Sect. 6.2. It is important to note that the remaining three cases (NGC 6790, IRAS 18240 and K 2-16) are the PNe with the highest continuum temperature among the PNe in our sample.

In Fig. 8, we compare the shape of the "30" μm profile of NGC 7027 with the profiles due to differently shaped MgS grains. As can be seen an oblate MgS grain with an axes ratio of 10:10:1 exhibits a "30" μm feature which peaks at the right position. At present we don't know of a physical reason for a preferred oblate grain shape in PNe, and a broader CDE shape distribution in the C-stars and post-AGB objects (see also Sect. 8.4).

The shape of a resonance is also influenced by the presence of a coating. MgS is very hygroscopic. Under conditions where oxygen is available in the gas phase MgS can be oxidised and transformed into MgO (Nuth et al. 1985; Begemann et al. 1994). It is possible that the MgS is transformed as the central star of the PN heats up and the UV radiation progressively dissociates the CO molecules yielding gas phase oxygen. This could lead to MgS grains which are coated by a thin layer of MgO. We have modelled such grains using the electrostatic approximation following Bohren & Huffman (1983, Chap. 5). The result is shown in Fig. 14, curve 6. As can be seen the "30" μm resonance is split into two features due to the MgO coating. The feature at the red wavelength is shifted to longer wavelengths compared to the pure MgS resonance. However the main feature is on the blue side of 25 μm towards the strong resonance at 18 μm in the pure MgO material, in clear contrast with the observations.

We explore other possible coatings on MgS grains to test their ability to explain the narrow feature observed in the PNe and the lack of emission at 26 μm. We find that of the composite grains we tested none give a satisfactory explanation. Mixtures of MgS and FeS have been discussed in the literature to investigate the nature of the "30" μm feature (Begemann et al. 1994; Men'shchikov et al. 2001; Henning 2000). Curves 1 and 2 in Fig. 14 show the result of embedding an FeS core in a mantle of MgS and embedding a MgS core in a mantle of FeS, respectively. The latter compares most favourably with the position of the feature in the PNe. However, the substructure found in the spectrum of the composite grain around 33−37 μm is not found in the PNe spectra.

Szczerba et al. (1999) examine grains of amorphous carbon with a mantle of MgS to compare with the 30 μm feature in two post-AGB objects. We show simulated spectra of such grains and MgS grains coated with amorphous carbon in Fig. 14, curves 3 and 4 respectively. Curve 3 clearly does not match the observed feature in the PNe. As can been seen in curve 4 the MgS grains coated with amorphous carbon absorb

less at 26 μm than pure MgS and are therefore a better spectral match to the "30" μm feature of the PNe. However, the feature to continuum ratio in these grains is about a factor 2.5 lower than in the pure MgS grains requiring a factor 2.5 more mass in the MgS component in order to explain the observed band strength. Note also that such grains will still produce a weak feature at 26 while in some PNe spectra we find no excess at that wavelength at all.

Lastly, in curve 5 (Fig. 14) we show the effect of water ice on the MgS grains. The effects on the optical properties of a water ice coating are marginal and the profile cannot explain the PNe observations. We conclude that of the composite materials we have experimented with MgS grains coated with amorphous carbon give the best spectral match. However we find no composite grains that match satisfactorily.

We stress that although our model does not reproduce the "30" μm profile in the PNe in its width it is safe to assume that *its carrier is MgS based*. These PNe are believed to be the evolutionary descendants of the sources which exhibit the MgS feature. The shift in peak position compared to the post-AGB objects follows naturally from an expanding and cooling shell. Also, the feature strength for the PNe is similar to these found in the post-AGBs further strengthening the physical link between the MgS in the C-stars and the post-AGBs on one hand and the "30" μm feature in the PNe on the other (see also Sect. 7).

7. Correlations

Using the large database of sources available we can study some of the properties of the "30" μm feature statistically. We have found it most convenient to characterise the sources by the temperature of the fitted continuum. We use the wavelength where the derived continuum peaks ($\lambda_{\rm max,cont}$) as an indicator of the continuum temperature. The derived continuum temperature itself is less well suited because of the systematic difference in the power law index we find between classes of sources. The sources are rather uniformly distributed over $\lambda_{\rm max,cont}$ as well.

First, we show in Fig. 15a the relation between the $\lambda_{\rm max,cont}$ and the ratio of the integrated flux in the "30" μm feature to the total flux in the SWS spectrum ($I_{30}/I_{\rm SWS}$). The C-stars demonstrate a clear increase of $I_{30}/I_{\rm SWS}$ with decreasing continuum temperature. The post-AGB objects emit systematically a larger fraction, of up to 25 per cent, in their "30" μm feature. The PNe emit a similar fraction in the "30" μm feature as the post-AGB objects although with a larger scatter. Notice that the sample contains a number of PNe with warm dust indicative of young PNe. There are a few sources which do not follow the general trend. The C-stars, R Scl, IRAS 19584 and RAFGL 2256, exhibit an atypically strong "30" μm feature. These latter two sources are further typified by very weak molecular absorptions near 14 μm (see also Fig. 3). These observed anomalies are indicative of deviating conditions in the outflows of these sources, possibly a recently halted period of efficient dust formation. The post-AGB object IRAS 19454 has a very weak and cold "30" μm feature. RAFGL 618 has a weak feature due to self-absorption (see Sect. 6.2).

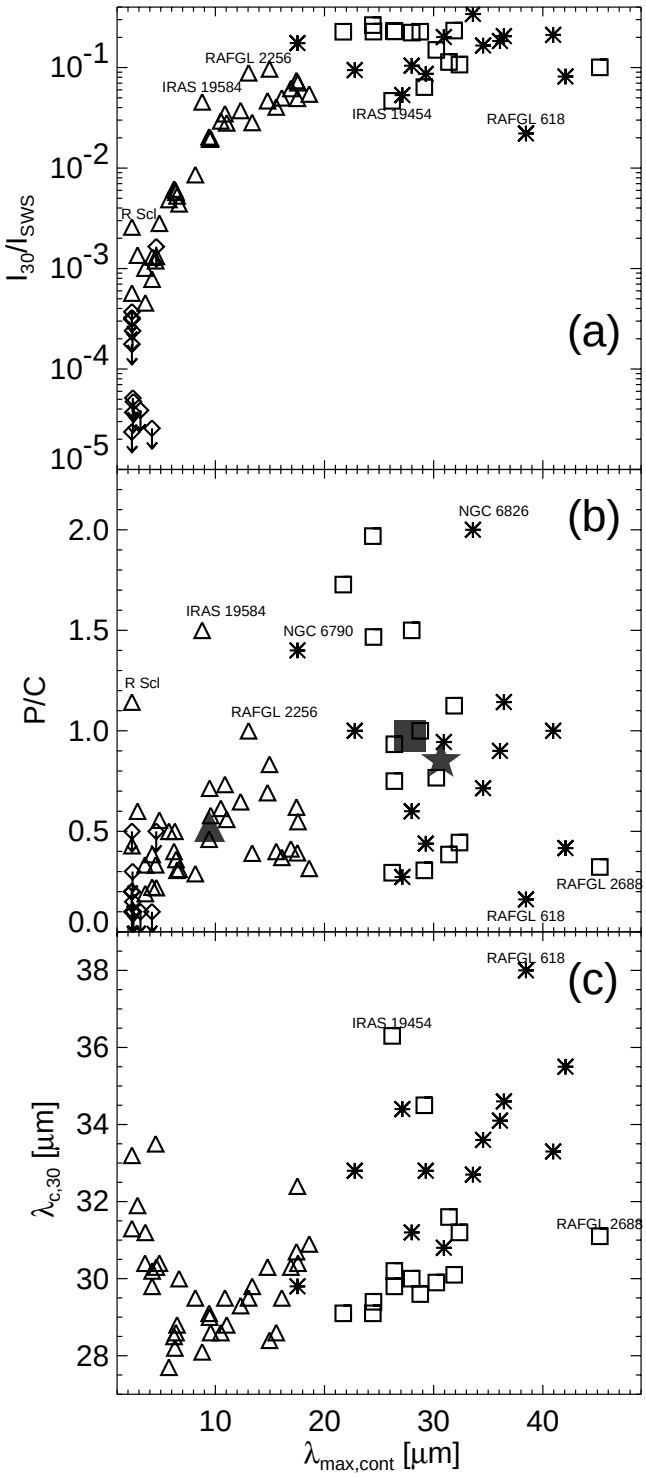

Fig. 15. "30" μm feature properties versus the peak wavelength of the continuum. The symbols are the same as in Fig. 1. We show in panel **a)** the ratio of the integrated flux in the "30" μm feature to the integrated flux in the SWS spectrum. In panel **b)**, we show the peak over continuum values. We also show the average values for the C-stars, the post-AGBs and the PNe. The non-detections are not taken into account in determining the mean values. The centroid wavelength of the "30" μm feature is shown in panel **c)**.

The increasing strength of the "30" μm feature in the AGB stars in not surprising. Since the emission is optically thin I_{30} is

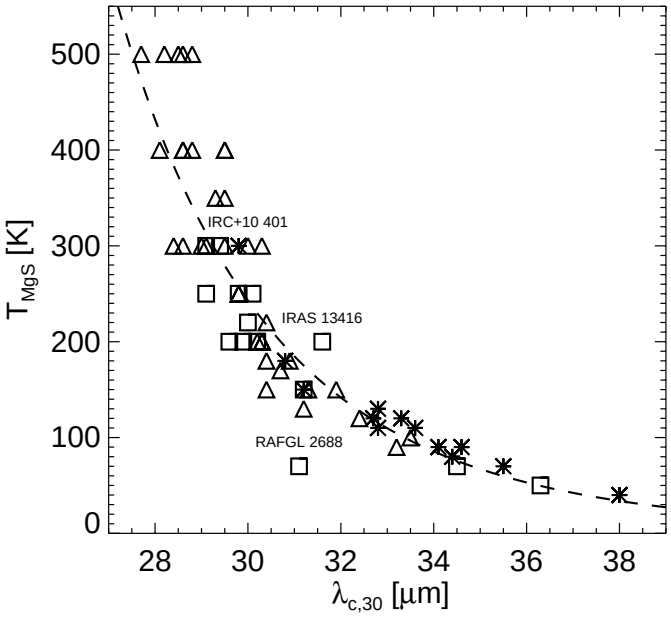

Fig. 16. The centroid position of the "30" μm feature versus the MgS temperature in the model. The symbols are the same as in Fig. 1. We show a power-law function fitted to the data with the dashed line.

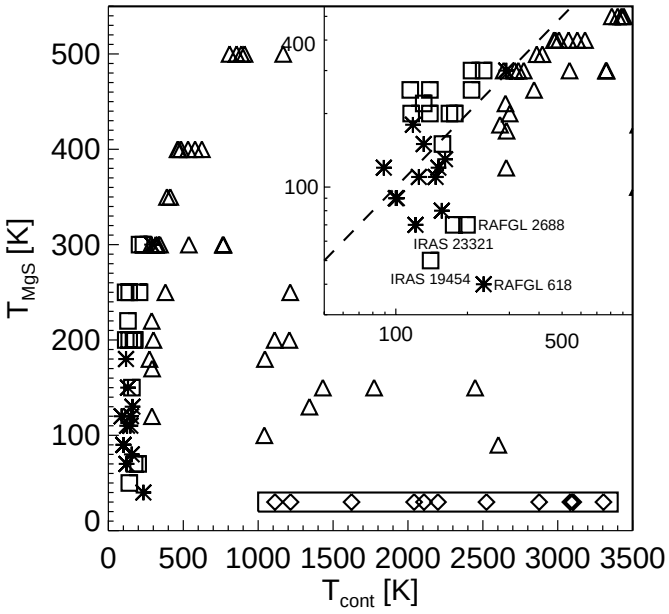

Fig. 17. The derived MgS temperature versus the continuum temperature. The symbols are the same as in Fig. 1. We show in the box in the lower right the continuum temperature of the sources without a "30" μm feature detected. The inset shows a blow up on a logarithmic scale up of the sources with a continuum temperature below 1000 K.

proportional to the amount of MgS. The low values of $I_{30}/I_{\rm SWS}$ for the warmest C-stars reflects the fact that there is little dust around these sources and most of the IR radiation comes from the stellar photosphere. Cooler C-stars have more dust and thus more MgS. The difference between the coolest C-stars and the post-AGBs is more surprising. The fact that post-AGBs emit a larger fraction in the "30" μm feature is due to two effects. First since the dust shell becomes optically thin in the visible some fraction of the light is emitted at shorter wavelengths. Second, the temperature of the MgS decreases less rapidly than the temperature of the other dust components (see below).

It is clear that any dust component which produces 30 per cent of the IR light has to be abundant. In order to quantify the (relative) amounts of MgS present in the CS shells of these objects will require radiative transfer modelling which is beyond the scope of this paper. We can however in first approximation study the relative amounts of MgS compared to the other cold dust components by studying the peak to continuum ratio (P/C). In Fig. 15b, we show the P/C versus the $\lambda_{\rm max,cont}$. The majority of the sources lies within the 0.3−1.0 range in P/C. We indicate a few clear outliers. R Scl, IRAS 19584 and RAFGL 2256 have a very strong "30" μm feature indicating again that these sources have "too much" MgS for a normal C-star. The PNe NGC 6790 and NGC 6826 have an exceptionally strong MgS feature. Note that NGC 6790 also has a very warm continuum, much like a post-AGB source or a very young PN. The strong SiC band at 11 μm is consistent with this. We also show the averages for each of the classes of sources. The average P/C for C-stars is 0.5, for post-AGB objects 1.0 and for the PNe it is 0.9. The similar ratios for the post-AGB objects and the PNe suggests that the carrier of the "30" μm feature in the PNe is indeed directly related to the MgS feature in the post-AGBs. Furthermore, the similar ranges found for the post-AGB objects and the PNe argues against any process which results in a destruction of the MgS grains during the PN phase.

In Fig. 16, we show the derived MgS temperature versus the centroid position of the "30" μm feature. The two are well correlated. For convenience, we have fitted a power-law function (without physical meaning) to the relation.

$$T_{\rm MgS} = 5.1 \times 10^{14}\ (\lambda_{\rm c,30})^{-8.34}\,. \quad (4)$$

It is not surprising that $T_{\rm MgS}$ and $\lambda_{\rm c,30}$ are correlated since we have used the feature profile to estimate the $T_{\rm MgS}$. However, using Fig. 16 or Eq. (4) one can easily derive the MgS temperature from a given observation. Also indicated in the figure are IRAS 13416 and RAFGL 2688; as can be seen they fall outside the correlation. This is due to the optical depth effects discussed above.

Lastly, we show in Fig. 17 the relation we find between the temperature of the continuum ($T_{\rm cont}$) and the temperature of the MgS ($T_{\rm MgS}$). We find, tracing the evolution from hot dust sources (C-stars) to the PNe, that the MgS temperature decreases correspondingly. Surprisingly, we find for warmest sources in the sample, with $T_{\rm cont} > 1000$ K, very cold MgS. We propose two explanations for this phenomenon. First, it may be due to the absorption properties of MgS. If MgS cannot efficiently absorb the stellar light in the optical or near-IR part of the spectrum the grains remain cold. Alternatively, the MgS grains may be located further away from the star (see below). In the inset, we show a blow-up of the left side of the figure. There is a clear correlation between $T_{\rm cont}$ and $T_{\rm MgS}$. The MgS in the post-AGB sources is systematically warmer than expected on the basis of the C-stars. Apparently, in the process of becoming a post-AGB object, when the dust shell becomes detached and moves away from the star, the general dust cools down more

rapidly than does the MgS. Note that the difference in dust temperature between the coldest C-stars and the warmest post-AGBs is seen most clearly in the [12]–[25] colour or $\lambda_{\rm max,cont}$ but is also found in the [25]–[60] colour (e.g. Fig. 1). The different behaviour of the continuum and the MgS is nicely illustrated in Fig. 15c where we show that while the continuum becomes redder the position of the "30" μm feature does not change. This effect is the cause for the discontinuity between the C-stars and the post-AGB object seen in Figs. 15a and b. The physical cause for this must be due to the fact that MgS is actually (partially) heated by mid-IR radiation. The mid-IR radiation is much slower to respond to the termination of the AGB. Conversely, this implies that mid-IR radiation is a less important heating agent for the other dust components present.

8. Discussion

8.1. Carrier

The models using MgS we present do very well in explaining the profile of the feature found in the C-stars and post-AGB objects. The model does not do as well in explaining the profile of the feature found in the PNe. However, the smooth relation found between the [25]–[60] colour and the $\lambda_{\rm c,30}$ shows a gradually changing profile with dust temperature. This suggests one carrier or closely related carriers. Also the similar P/C values for the different classes of objects is indicative of one carrier.

Recently Grishko et al. (2001) proposed HAC as the carrier of the mid-IR emission features in C-stars, post-AGBs and PNe. HAC is a very plausible dust component in those environments (e.g. Duley & Williams 1981; Goebel 1987; Borghesi et al. 1987; Henning & Schnaiter 1999). However, the mid and far-IR optical properties of HAC are dominated by a λ^{-1} continuum (Bussoletti et al. 1987). Grishko et al. (2001) identified some 13 weak spectral features in the range from 19−120 μm. The strongest of which occur at 21, 27 and 57 μm. We consider HAC a unlikely candidate for the circumstellar "30" μm emission feature because the laboratory features are weak in contrast to the astronomical data and because the far-IR features of HAC are not observed in the astronomical spectra.

8.2. The effect of model simplifications

It is remarkable that our simple model works so well. We have applied various simplifications in order to be able to study the whole sample in a unified way. These simplifications necessarily lead to differences between the models and the observations. Instead of assuming a single temperature modified blackbody for the shape of the continuum one can certainly obtain a more detailed fit by taking into account the structure of the CS envelope and the opacities of the different molecular and dust constituents. Our method works well because the contributions of the other known other dust components around 30 μm are well behaved, smooth and thus indeed form a continuum. Moreover, the shape of our modelled continuum between 20−50 μm is not a strong function of the emissivity index (p) and varying the p-parameter or the temperature doesn't yield qualitatively different continuum shapes or levels. We already pointed out that in some cases our model fails at the longest wavelengths of the SWS observations, which may be related to our method to estimate the continuum.

We use a single temperature for the MgS to model its contribution. In the very extended envelope of a C-star or in the nebulous environments in the post-AGBs and PNe, the temperature of any dust component will not be constant but decreases as a function of the distance to the star. The fact that we still get good results using a single temperature is a clear indication that the emission is optically thin and that the density of the MgS falls off sharply with distance. In an optically thin environment we know that $T_{\rm dust} \propto \sqrt{R}$, where R is the distance to the star. If the density distribution drops with distance as R^{-2} or steeper, the contributions are weighted to the highest temperature part of the envelope where $T_{\rm dust}$ and thus the source function is highest. If the density distribution is flatter there is relatively more dust far away than close by. In this case we will observe MgS with a range of temperatures. Also sources that are not optically thin will emit a feature broader than our single temperature MgS model (see also Sect. 6.2). We conclude that in the majority of the sources the "30" μm emission is due to optically thin emission which is dominated by the highest temperature MgS closest to the star.

8.3. Shape

We find that a CDE shape distribution fits many observations well. A CDE shape distribution is used to model a collection of irregularly shaped grains. Irregularly shaped grains can for example result from grain growth by agglomeration (Blum et al. 2000).

We find evidence for differences in the shape distributions between sources. We have tested for correlations between the strength of the 26 μm excess (due to spherical MgS grain) and the CDE component and other parameters like the mass-loss rate, the P/C, the continuum temperature or the feature temperature. We find no clear correlations. We do however note that we find little evidence for the 26 μm excess in the hottest C-stars. Stars in our sample with a continuum temperature above 1000 K do not exhibit the excess. Below 1000 K we find both sources with and without the 26 μm excess. Note also that the occurrence rate of the 26 μm excess in the sample of post-AGB objects is high. Because the emission in the post-AGB phase may be dominated by the dust closest to the star and hence lost at the tip of the AGB during a phase of heavy mass loss (at a rate much higher than during the general AGB phase), this might suggest that the shape distribution of the grains changes to become more spherical towards the end of the AGB, possibly as a function of mass-loss rate.

8.4. Planetary nebulae

The profile of the "30" μm feature we find in most PNe is narrower than in our model. The largest discrepancy occurs around 26 μm. Our model fits are able to explain the shift in centroid position observed in the PNe; however, the models that explain the band-shift best, over-predict the flux at 26 and 40 μm.

There are several observational properties that are important when considering explanations for the observed discrepancies. First, there is the similar values of P/C in the sample of post-AGBs and PNe (Fig. 15b). This indicates that the carriers are related and similar in abundance. Second, the smooth trend we find in the centroid position of the "30" μm feature with the [25]–[60] colour (Fig. 6). The PNe profiles follow the general trend. This indicates that the main effect for the peak shift *also in the PNe* is due to temperature. We also note that there are three non-PNe sources in our sample with cold MgS (R Scl, IRAS 19454 and IRAS 23321). These sources are well fitted by our model. This indicates that the narrow profiles are particular to the PN environment.

We have explored possible MgS based heterogeneous grains and variations in MgS grain shape. The heterogeneous grains we have explored do not compare satisfactorily with the observed profile in the PNe. MgS grains coated with a layer of amorphous carbon provide a somewhat better match in terms of the band shape however the contrast of the feature with respect to the continuum is strongly reduced. The reduced band strength is in contradiction with the observed peak over continuum ratios.

We find that the emission from plate-like MgS grains appears similar to the feature found in the PNe. In Sect. 6.1 we consider an extra contribution of spherical MgS grain to the "30" μm feature at 26 μm. The varying strength of this contribution demonstrates that there are variations in the grains shape distribution between sources. The question is: "Is it possible that the narrow "30" μm feature in the PNe is carried by flattened MgS grains?" This would either imply that the MgS grain shape distribution in the PNe is heavily skewed to the plate-like grains or that the oblate grains emit more efficiently.

The origin of these variations in the shape distribution are unclear. They may reflect variations in the formation and destruction of grains. We do not know of a mechanism that drives towards oblate grains shapes during the PN-phase or a mechanism that selectively destroys spherical and prolate grains. Note, that the peak over continuum value in the PNe is similar to those found in the post-AGB objects arguing against a destruction of a part of the MgS grains. It is important to remark that in the CDE distribution only ~20 per cent of the grains is oblate with an axis ratio of $1{:}\frac{1}{5}$ or more extreme, i.e. with axes ratios of $1{:}X{:}Y$, where Y is smaller than $\frac{1}{5}$ and X can vary between $\sqrt{X}$ and 1. Such axes ratios are required in order to shift the peak position to the wavelength where the "30" μm feature in the PNe peaks and to suppress the emission at 26 μm.

Alternatively, these inferred shape variations may result from a shape dependent heating of grains. In the C-stars, likely, heating and cooling occurs at IR wavelengths. Because the grains are small compared to these wavelengths the temperature will be shape independent. However, in the PNe heating occurs through absorption of visible and UV radiation, which scales with the cross-section. Hence in that case dust temperatures will be shape dependent. Indeed flattened grains have on average a larger geometric cross-section compared to their volume that spherical or prolate grains.

As noted before, the PNe in the sample with the warmest dust continuum are well fitted by our model. The model fails in the PNe sample at MgS temperatures below ~90 K. Perhaps, the observed discrepancies are due to changes in the optical properties of pure MgS at low temperatures. No laboratory measurements of MgS at these temperatures are published. FeO has the same lattice structure as MgS and measurements of FeO at different temperatures (10 K, 100 K, 200 K and 300 K) are available (Henning & Mutschke 1997). We have used FeO as an analogue to examine the effect of temperature. The trend with lower temperature is for the FeO resonance at 20 μm to become narrower and stronger with respect to the continuum. There is a small shift in the peak position. Comparing the 300 K measurement to 10 K the latter resonance peaks ~0.1 μm more to the blue for spherical grains. Like MgS, FeO is also very sensitive to the shape of the grains. Using a CDE shape distribution the resonance of the 10 K sample lies ~1 μm on the blue side of the 300 K resonance. If we translate this behaviour to the MgS data and the "30" μm feature in the PNe it worsens the situation since we would expect a stronger contribution at shorter wavelengths exactly where our model already over-predicts. As an alternative, one might speculate that a change in lattice structure at low temperatures may occur resulting in different optical properties. It is interesting to note that Berthold (1964) reports that MgS can condense in two lattice structures: cubic and hexagonal. This author finds that hexagonal MgS exhibits a narrower mid-IR resonance than cubic and amorphous MgS.

We conclude that, although it is possible to find MgS based candidate materials that provide a better spectral match to the observed "30" μm feature in the PNe no explanation for the "30" μm profiles in the PNe is completely satisfactory at this time.

8.5. MgS temperature

We have found that the "30" μm feature is very well explained with MgS provided that the continuum temperature and the MgS can be substantially different from each other (see also Fig. 17). Moreover, the temperature difference changes between classes of sources. In the C-stars we find that MgS is colder than the continuum while in the post-AGB sample the MgS grains are warmer. The temperature difference and the fact that the continuum temperature varies relative to the MgS temperature implies that the MgS grain are not in thermal contact with the amorphous carbons grains that carry the continuum. Thus, MgS is condensed in these environments into separate grains.

The relatively warm hot MgS that we observe in the post-AGB sample is certainly a phenomenon that deserves further study. As pointed out above, this must be due to a difference in the heating properties of MgS relative to the other dust constituents. We suggest that due to the strong resonance in the mid-IR MgS is (partially) heated by IR radiation. This may cause a temperature difference as observed. It requires measured optical constants for MgS over a much wider wavelength range than now available and radiative transfer modelling to

understand the detailed temperature behaviour of the MgS grains.

We have shown in Fig. 17 that the warmest C-stars that exhibit the "30" μm feature have cold MgS. We consider two possible explanations for this behaviour. First, MgS can be cold because it is unable to absorb the radiation from the central source efficiently. This would require that the MgS grains are very transparent in the visible and near-IR where these warm C-stars emit most of their radiation. In this case a *cooler* star will emit more radiation at wavelengths where MgS can absorb and as a result the MgS grains will be *warmer*. This explanation is consistent with our notion that MgS is (partially) heated by IR radiation.

A second intriguing possibility is that the MgS around these sources is located far away from the star. R Scl, U Cam and W Ori are known to have a detached dust shell (Zuckerman 1993). These shells are formed during an earlier phase when the mass-loss rate was higher than the current mass-loss rate (Willems & de Jong 1988). If during this phase the AGB star was already a C-star, MgS could have condensed in the outflow and be present in the detached shell. We have sketched in Fig. 1 the evolution of a star which suffers a brief period of enhanced mass loss. First, the star becomes redder during the phase of high mass loss. When the shell becomes detached the 12 μm flux quickly drops while the inner edge of the dust shell moves away from the star and the warmest dust is rapidly lost. The star moves back to the locus of the warmest C-stars but with an excess of cold dust. The excess of cold dust is observable as a 60 μm excess. The sources mentioned above indeed show the 60 μm excess. We note that some stars with 60 μm excess do not show the "30" μm feature.

To distinguish between these two possibilities requires radiative transfer modelling and a more detailed investigation of these particular sources which is beyond the scope of this paper. The location and temperature of the MgS in the warmest C-stars will be further discussed in a forthcoming paper (Hony et al., in prep.).

8.6. MgS in the ISM

The behaviour of the MgS we find in this study has implications for our understanding of the fate of MgS that is produced during the C-star phase. Previously, the existence of MgS in the ISM has been excluded because of the lack of spectral signature at 26 μm. We have shown that at low dust temperatures no emission signature is expected at 26 μm. For the dust temperatures in the ISM we would expect a smooth feature at wavelengths longer than 35 μm. In this respect it is interesting to note that the peak to continuum (P/C) values in the post-AGB and PNe sample are similar. We find no evidence for a rapid destruction by the UV radiation field in the PN. This shows that the MgS will indeed be injected into the ISM. Of course, in the ISM the contrast will be much less because the injected material will be diluted with other star-dust and general ISM material. Nevertheless a search for the "30" μm feature in the ISM may be very worthwhile. In this respect it is important to note that Chan et al. (1997) have discussed a broad emission feature they observed along several lines of sight towards the galactic centre. The feature they observed is similar to the "30" μm feature observed in the C-rich post-AGB objects.

9. Summary and concluding remarks

We present a large sample of 63 ISO/SWS spectra of carbon-rich evolved objects that exhibit a "30" μm feature. The feature is detected along the complete evolutionary track from low mass loss C-stars and extreme C-stars via post AGB objects to PNe.

We present a simple approach to determine the continuum. We study the profile of the "30" μm feature after continuum subtraction. We find large systematic variations in the appearance of the "30" μm feature. We firmly identify the carrier of the feature with MgS in a CDE shape distribution. The profile of the observed feature is consistent with MgS provided that the temperature of the MgS can be different from the bulk of the dust. This approach allows us to model, in a unified way, the profiles of the "30" μm feature in a wide range of objects even when the feature can appear extremely different.

We find an additional component at 26 μm in ~25 sources. We argue that this component is due to differences in the distribution over shapes of the MgS grains; specifically, it requires a distribution more weighted to spherical MgS grains. We find no clear correlations of this excess with other properties of the sources. The self-absorbed "30" μm features of RAFGL 618 and RAFGL 2688 reflect the high optical depth in the "30" μm feature in these sources.

We find that the typical profile of the "30" μm feature in the PNe is narrower than predicted by our model. We consider several possible explanations. We find that flattened MgS grains provide a better spectral match to the "30" μm feature in the PNe. However it is presently unclear why in the PNe environment the "30" μm feature is dominated by flattened grains.

We find that the temperature of the MgS grains is different from the bulk of the dust. Therefore, they cannot be in thermal contact with the other dust species but must exist as separate grains. In the C-stars MgS is colder than the other dust while in the post-AGB objects MgS is warmer. Likely, this is because the MgS is efficiently heated by mid-IR radiation which is less important in the C-stars.

The behaviour of the temperature of the MgS for the hottest C-stars is enigmatic. The hottest sources have very cold MgS grains. We propose two explanations for this phenomenon. First, the "30" μm feature in these sources may be due to a previous mass-loss phase and the MgS is thus located far from the source and cold. Second, the MgS grains absorb very inefficiently in the optical and near-IR and therefore the hottest C-stars do not heat the MgS grains well.

We examine the feature over continuum ratio to study the relative proportion of MgS to the other dust components. We find no evidence for rapid destruction of MgS grains during the PNe phase and possibly MgS grains may survive to be incorporated into the ISM.

We would like to emphasise the need for further measurements of the optical properties of astrophysically relevant materials at *all relevant* wavelengths. This study has put forwards some very interesting questions in relation to the absorption

properties of MgS in the optical and near-IR and also concerning low temperature effects. Unfortunately, no published laboratory measurements are available to test some of our scenarios and conclusions.

Acknowledgements. SH and LBFMW acknowledge financial support from NWO *Pionier* grant 616-78-333. This research has made use of the SIMBAD database, operated at CDS, Strasbourg, France. This research has made use of NASA's Astrophysics Data System Bibliographic Services. IA^3 is a joint development of the SWS consortium. Contributing institutes are SRON, MPE, KUL and the ESA Astrophysics Division.

References

Begemann, B., Dorschner, J., Henning, T., Mutschke, H., & Thamm, E. 1994, ApJ, 423, L71
Berthold, G. 1964, Zs. Phys., 181, 333
Blum, J., Wurm, G., Kempf, S., et al. 2000, Phys. Rev. Lett., 85, 2426
Bohren, C. F., & Huffman, D. R. 1983, Absorption and scattering of light by small particles (New York: Wiley, 1983)
Borghesi, A., Bussoletti, E., & Colangeli, L. 1987, ApJ, 314, 422
Bussoletti, E., Colangeli, L., & Borghesi, A. 1987, in Polycyclic Aromatic Hydrocarbons and Astrophysics, NATO ASIC Proc., 191, 63
Cernicharo, J., Heras, A. M., Pardo, J. R., et al. 2001, ApJ, 546, L127
Chan, K., Moseley, S. H., Casey, S., et al. 1997, ApJ, 483, 798
Cox, P. 1993, in Astronomical Infrared Spectroscopy: Future Observational Directions, ASP Conf. Ser., 41, 163
de Graauw, T., Haser, L. N., Beintema, D. A., et al. 1996, A&A, 315, L49
Duley, W. W. 2000, ApJ, 528, 841
Duley, W. W., & Williams, D. A. 1981, MNRAS, 196, 269
Forrest, W. J., Houck, J. R., & McCarthy, J. F. 1981, ApJ, 248, 195
Goebel, J. H. 1987, in Polycyclic Aromatic Hydrocarbons and Astrophysics, NATO ASIC Proc., 191, 329
Goebel, J. H., & Moseley, S. H. 1985, ApJ, 290, L35
Grishko, V. I., Tereszchuk, K., Duley, W. W., & Bernath, P. 2001, ApJ, 558, L129
Guillois, O., Nenner, I., Papoular, R., & Reynaud, C. 1996, ApJ, 464, 810
Henning, T. 2000, ISO beyond the peaks: The 2nd ISO workshop on analytical spectroscopy, ed. A. Salama, M. F. Kessler, K. Leech, & B. Schulz, ESA-SP, 456, 329
Henning, T., & Mutschke, H. 1997, A&A, 327, 743
Henning, T., & Schnaiter, M. 1999, Earth Moon and Planets, 80, 179
Hony, S., Bouwman, J. B., Keller, L. P., & Waters, L. B. F. M. 2002, A&A, submitted
Hony, S., Waters, L. B. F. M., & Tielens, A. G. G. M. 2001, A&A, 378, L41
Hrivnak, B. J., Volk, K., & Kwok, S. 2000, ApJ, 535, 275
Jiang, B. W., Szczerba, R., & Deguchi, S. 1999, A&A, 344, 918
Kaler, J. B., & Jacoby, G. H. 1991, ApJ, 372, 215
Keller, L. P., Hony, S., Bradley, J. P., et al. 2002, Nature, 417, 148
Kessler, M. F., Steinz, J. A., Anderegg, M. E., et al. 1996, A&A, 315, L27
Kwok, S., Volk, K., & Bernath, P. 2001, ApJ, 554, L87
Latter, W. B., Dayal, A., Bieging, J. H., et al. 2000, ApJ, 539, 783
Lattimer, J. M., Schramm, D. N., & Grossman, L. 1978, ApJ, 219, 230
Lodders, K., & Fegley, B. 1999, in Asymptotic Giant Branch Stars, IAU Symp., 191, 279
Mendez, R. H., Kudritzki, R. P., & Herrero, A. 1992, A&A, 260, 329
Men'shchikov, A. B., Balega, Y., Blöcker, T., Osterbart, R., & Weigelt, G. 2001, A&A, 368, 497
Nuth, J. A., Moseley, S. H., Silverberg, R. F., Goebel, J. H., & Moore, W. J. 1985, ApJ, 290, L41
Omont, A. 1993, in Astronomical Infrared Spectroscopy: Future Observational Directions, ASP Conf. Ser., 41, 87
Omont, A., Moseley, S. H., Cox, P., et al. 1995, ApJ, 454, 819
Papoular, R. 2000, A&A, 362, L9
Perinotto, M. 1991, ApJS, 76, 687
Quigley, M. F., & Bruhweiler, F. C. 1995, in American Astronomical Society Meeting, 187, 8008
Szczerba, R., Henning, T., Volk, K., Kwok, S., & Cox, P. 1999, A&A, 345, L39
van der Veen, W. E. C. J., & Habing, H. J. 1988, A&A, 194, 125
Volk, K., Kwok, S., Hrivnak, B. J., & Szczerba, R. 2002, ApJ, 567, 412
Volk, K., Xiong, G., & Kwok, S. 2000, ApJ, 530, 408
von Helden, G., Tielens, A. G. G. M., van Heijnsbergen, D., et al. 2000, Science, 288, 313
Waters, L. B. F. M., Molster, F. J., Hony, S., et al. 2000, Thermal Emission Spectroscopy and Analysis of Dust, Disks, and Regoliths, ASP Conf. Ser., 196, 3
Willems, F. J., & de Jong, T. 1988, A&A, 196, 173
Yamamura, I., De Jong, T., Justtanont, K., Cami, J., & Waters, L. B. F. M. 1998, Ap&SS, 255, 351
Young, K., Phillips, T. G., & Knapp, G. R. 1993, ApJS, 86, 517
Zuckerman, B. 1993, A&A, 276, 367